Semester Project

ETH Zürich

Low Frequency Resonators on Superconducting Chips

A Space-Efficient Lumped Element Design

Authors:
Patrick M. Lenggenhager,
Bradley Mitchell

Supervisors:
Prof. Dr. Andreas Wallraff,
Dr. Anton Potočnik

October 18, 2015

Abstract

The interest in engineering HF- and VHF-band (3 to 300 MHz) superconducting resonators is motivated by the potential low-loss character of quantum optical devices in this frequency regime. Required to utilize resonators in this frequency regime is an active cooling technique that is well known in the field of optomechanics. In principle, technologies exist to simulate an all-electrical optomechanic-like interaction between a microwave resonator and a low-frequency resonator. However, the development of a space-efficient low-frequency resonator is needed.

Several different geometries for achieving space-efficient low frequency resonators on superconducting chips have been considered and compared. An optimized lumped element design, called a *pack arranged* resonator, a simple parallel non-grounded LC resonator, is proposed and was fabricated, measured and compared to low frequency resonators of the established coplanar waveguide type. The frequency range 300 MHz to 6 GHz was investigated.

In the investigated frequency range the design accuracy of the simple LC resonator model is determined to be sufficient for frequency in that the maximal errors were on the order of 10%, however, a systematic and consistent mismatch in the coupling rate has been observed. This could be explained by additional capacitance to ground. The loss rate is found to be decreasing with decreasing frequency according to a power law, whereas no clear trend is identifiable in the case of CPW resonators. The spectra of spurious modes, which most likely are due to self resonance phenomena, show a large gap between the fundamental resonance and the first spurious mode.

In addition, a satisfactory design accuracy in fundamental frequency, coupling capacitance and higher order modes in the case of coplanar waveguide resonators in the frequency range of 200 MHz to 1.5 GHz is demonstrated.

Contents

List of Figures

Chapter 1

Introduction

A new frequency range (3 to 300 MHz) of superconducting resonators offers potential for quantum optical devices with longer photon lifetimes. Beyond design challenges concerning size constraints of such devices, the transition energy of these low-frequency (LF) resonators is comparable to the thermal occupation of a dilution refrigerator. Therefore, an active cooling technique, well known in the field of optomechanics, must be engineered to operate LF resonators with low thermal excitation. In principle, technologies exist to realize an all-electrical optomechanic-like interaction between a microwave and a low-frequency resonator. In this chapter, we briefly discuss why low frequency resonators are appealing to QuDev and relevant experiments for which their properties can be used, including the optomechanic-like interaction.

1.1 Low Frequency Resonators

Low frequency resonators do have some advantages in circuit quantum electrodynamics. A recent experiment exploring multimode strong coupling [4] required a low-frequency resonator to couple a qubit to many nondegenerate cavity modes, for example. They are expected to be less lossy, as resistivity from quasiparticles in superconductors scales as $\rho_{SC} \propto \omega^2$ [18], and can therefore be useful as selective filters. They can also be coupled to systems that require low frequencies. They could enable longer storage of quantum information and are good candidates for a hybrid setup for quantum computation, where different qubit realizations are used for storing and processing tasks (e.g. *Transmon* qubits for processing and nuclear spin states for storing information). Lower loss devices could also be achieved because of the availability of low-noise electronics in this frequency regime. However, resonators of lower frequency usually require very large structures composed of small structures, which may pose some problems. The goal of this work is to consider different possible designs of low frequency resonators and propose one particular design. Some initial investigation on this design is done and compared to the more established coplanar waveguide resonator with particular interest in the sub-GHz frequency range.

An additional problem when using low frequency resonators for quantum computation is the fact they are more easily thermally excited; to put them in

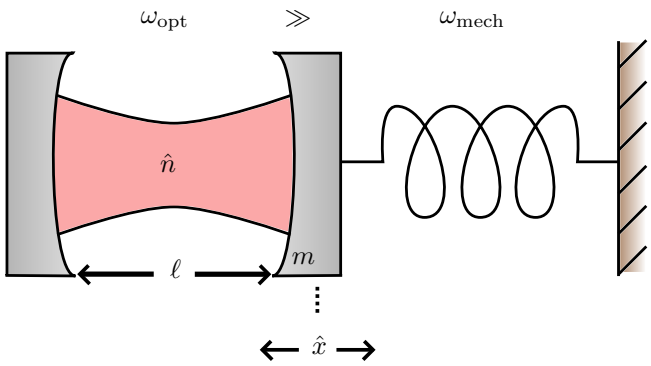

Figure 1.1: Schematic of an optomechanical system. The optical cavity's resonance ω_{opt} is shifted by the displacement $\hat{x}$ of the mechanically compliant mirror of mass m and frquency ω_{mech}. This coupling and the frequency difference between each oscillator are what mathematically identify optomechanical systems.

the ground state, lower temperatures are required. For fundamental transition frequencies of a few hundred Megahertz the ground state temperature is around 5 mK, below the temperature of a usual dilution cryostat ($T_{\text{cryo}} \approx 20\,\text{mK}$). As an alternative to a more elaborate external cooling, active cooling methods are a viable solution (see section 1.2).

1.2 Optomechanics Analogy

Microwave-frequency resonators have transition energies orders of magnitude greater than the thermal energy of their environment in a dilution cryostat. Because of this, microwave resonators can be externally cooled to their ground state. As stated above, this is no longer true once the transition energies are in the VHF-band of hundreds of Megahertz. Thus, to take advantage of the benefits for such low-frequency resonators outlined in section 1.1, we must have the ability to actively cool them to their ground-state. In the trapped ion community, experimental methods to cool the mechanical modes of the atomic center-of-mass motion of the ions is necessary due to ambient temperatures higher than the fundamental transition energy of the atomic motion [20]. This method is known as sideband cooling and has been done on mechanical systems with comparable frequency to our interest using microwave resonators [17].

Sideband cooling utilizes a particular coupling between a high-frequency and a low-frequency resonator. The classic example, seen in figure 1.1, consists of an optical cavity with one mirror that is mechanically compliant. The displacement of the mirror changes the resonance frequency of the cavity because the cavity length is inversely proportional to its frequency. This gives a Hamiltonian which can be written as [1]

$$\hat{H} = \hat{H}_{\text{mech}} + \hbar\left(\omega_{\text{opt}} + g_{\text{om}}\hat{x}\right)\hat{n}, \tag{1.1}$$

where $\hat{n}$ is the number of photons in the cavity and $g_{\text{om}} = \frac{\partial\omega_{\text{opt}}}{\partial x}$ is the optomechanical coupling obtained by a first-order Taylor expansion of $\omega_{\text{opt}}(x)$.

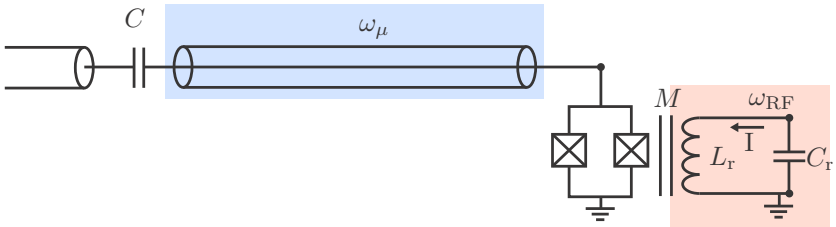

Figure 1.2: An example circuit schematic for an all-electrical optomechanically-coupled device. In blue is a microwave CPW resonator terminated with a SQUID loop to ground. This is coupled inductively with mutual inductance M to the radio-frequency (RF) lumped-element resonator in red.

This type of coupling can also be engineered between two superconducting resonators [8]. A circuit schematic of the device design is shown in figure 1.2. It consists of a high-frequency (HF) oscillator with a SQUID loop contributing to its inductance. Note that the HF oscillator is a transmission-line resonator in the figure. This need not be the case–alternative geometries are also possible, such as a lumped element device. The mutual inductance M between the loop and the low-frequency mechanical-like resonator realizes the coupling between amplitude $\hat{\phi} = M\hat{I}$ of the LF resonator and the HF resonator, as the flux through the SQUID loop changes its inductance, and therefore the resonant frequency of the device.

1.2.1 Sideband Cooling an RF Resonator

As mentioned above, a device such as depicted in figures 1.1 or 1.2 can be used to actively cool the LF resonator in the system. A schematic of sideband cooling is shown in figure 1.3. The basic process is as follows: one applies a drive to the system ω_d, and this drive produces sidebands $\omega_d \pm \Omega_m$ in the output on either side of the drive tone spaced by the mechanical resonance Ω_m. These are the Stokes $(-)$ and anti-Stokes $(+)$ sidebands. By choosing the drive frequency to be below the HF resonator resonance by Ω_m, the cavity filters the Stokes peak, and passes the anti-Stokes peak. As given in the figure, the scattering rates $\Gamma_\pm$ to the Stokes $(-)$ and anti-Stokes $(+)$ sidebands become asymmetric, with $\Gamma_+ \gg \Gamma_-$. This asymmetry results in upconversion of drive photons, whose energy is derived from the motion of the mechanical oscillator. This constitutes an active cooling mechanism of the resonator, and experiments have been done to observe the quantum asymmetry of these peaks for mesoscopic mechanical oscillators by cooling in this way [14].

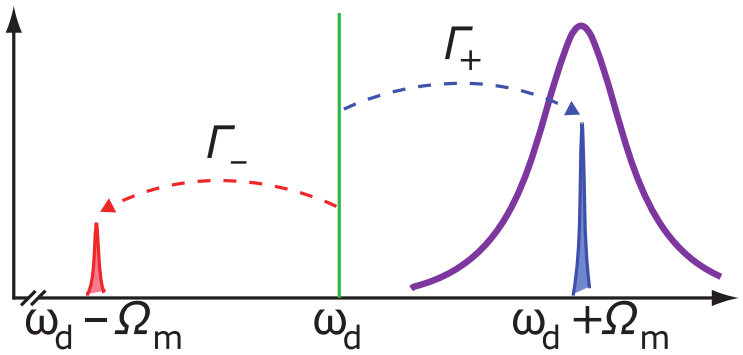

Figure 1.3: Schematic of sideband cooling. The drive ω_d produces sideband resonances spaced by the mechanical resonances at $\pm\Omega_m$. When detuning the drive by Ω_m, the anti-Stokes sideband is retained while the cavity scatters photons to the anti-Stokes band at rate Γ_+ and to the Stokes band at rate Γ_-. This asymmetry in energy scattering extracts excitations from the mechanics, thereby cooling it. Figure edited from [17].

Chapter 2

Theoretical Considerations

In this chapter the theoretical considerations regarding different resonator types as well as the models used to describe, optimize and design them are presented. This includes aspects relevant for the choice of certain design parameters as well as those that are necessary to determine the geometrical for given physical design parameters.

There are several different types of planar resonators, such as coplanar waveguide (CPW), lumped element (LE) and spiral resonators. In this chapter first two are introduced, compared and described in detail. Furthermore some estimates for how suitable they could be as low frequency resonators are presented. The circuits in consideration are based on superconducting transmission lines placed on chips. The main criteria for selecting the optimal resonator types are space-efficiency, simplicity with respect to fabrication and compatibility with existing experimental setups at the *Quantum Device Lab* (QuDev) at ETHZ[1].

2.1 Resonator

2.1.1 Quantum LC Oscillator

The electrical circuit shown in figure 2.1, that is an LC oscillator circuit, is considered. With respect to the position variable q the Lagrangian is

$$\mathscr{L} = \frac{1}{2}L\dot{q}^2 - \frac{1}{2}\frac{q^2}{C} = \mathscr{L}(q, \dot{q}). \tag{2.1}$$

The conjugate momentum to q is

$$\frac{\partial \mathscr{L}}{\partial \dot{q}} = L\dot{q} = LI = \Phi. \tag{2.2}$$

The Legendre transform then gives the Hamiltonian

$$\mathscr{H}(q, \Phi) = \Phi \cdot \frac{\Phi}{L} - \mathscr{L}\left(q, \frac{\Phi}{L}\right) = \frac{1}{2L}\Phi^2 + \frac{1}{2C}q^2. \tag{2.3}$$

[1] The laboratory in which this investigation was conducted.

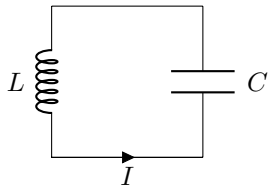

Figure 2.1: A circuit with an inductance L and capacitance C is an LC oscillator. The flux through the inductor is denoted by Φ, the charge on the capacitor plates $\pm q$ and the current flowing through the circuit by $I = \dot{q}$.

The LC oscillator can then be quantized using second quantization, that is q, Φ are replaced by operators $\hat{q}, \hat{\Phi}$ that satisfy the canonical commutator relation $\left[\hat{q}, \hat{\Phi}\right] = i\hbar$ and the creation and annihilation operators

$$\hat{a} = \sqrt{\frac{Z}{2\hbar}}\hat{q} + i\sqrt{\frac{1}{2\hbar Z}}\hat{\Phi}, \tag{2.4a}$$

$$\hat{a}^\dagger = \sqrt{\frac{Z}{2\hbar}}\hat{q} - i\sqrt{\frac{1}{2\hbar Z}}\hat{\Phi}. \tag{2.4b}$$

with the oscillator impedance $Z = \sqrt{\frac{L}{C}}$. They satisfy the necessary commutator relation $\left[\hat{a}, \hat{a}^\dagger\right] = 1$. Defining the number operator $\hat{n} := \hat{a}^\dagger\hat{a}$ and expressing impedance with resonance frequency $Z = \omega_0 L$ allows the Hamiltonian to be written as

$$\mathscr{H} = \hbar\omega_0\left(\hat{n} + \frac{1}{2}\right), \tag{2.5}$$

which is recognized as the Hamiltonian of the usual quantum harmonic oscillator with frequency ω_0.

The operators for charge and flux can be written using equation (2.4) as

$$\hat{q} = \sqrt{\frac{\hbar}{2Z}}\left(\hat{a} + \hat{a}^\dagger\right), \tag{2.6a}$$

$$\hat{\Phi} = -i\sqrt{\frac{\hbar Z}{2}}\left(\hat{a} - \hat{a}^\dagger\right), \tag{2.6b}$$

which allows the calculation of the ground-state uncertainties

$$\Delta\hat{q} = \sqrt{\langle 0|\hat{q}^2|0\rangle - \langle 0|\hat{q}|0\rangle^2} \quad = \sqrt{\frac{2\hbar}{Z}} = q_{\mathrm{ZPF}}, \tag{2.7a}$$

$$\Delta\hat{\Phi} = \sqrt{\langle 0|\hat{\Phi}^2|0\rangle - \langle 0|\hat{\Phi}^2|0\rangle^2} = \sqrt{2\hbar Z} = \Phi_{\mathrm{ZPF}}, \tag{2.7b}$$

which are sometimes called *zero-point fluctuations*.

2.2 Coplanar Waveguide Resonators

2.2.1 Fundamental Frequency and Spectrum

A coplanar waveguide resonator (CPW), which is based on a simple stripline, can be considered as a quasi-one-dimensional transmission line cavity. In the

transmission line of length l standing waves form and the fundamental frequency of the $\lambda/2$-waves is given by [7]

$$f_0 = \frac{c}{\sqrt{\varepsilon_{\text{eff}}}} \frac{1}{2l}, \tag{2.8}$$

which can trivially be found via $l = \lambda_0/2$ for two-ended resonators, and the phase velocity $v_{\text{ph}} = c/\sqrt{\varepsilon_{\text{eff}}}$, where c is the speed of light and ε_{eff} the effective permittivity of the CPW line. The effective permittivity depends on the geometry of the stripline (see section 2.2.2). These resonators, due to their quasi-one-dimensional boundary conditions, admit higher-order resonances in intervals of the fundamental frequency, with each additional mode containing an another field node along the structure.

The most important parameter for CPW resonators is their length. As the fundamental frequency scales linearly with the inverse of the length, long transmission lines are required in order to achieve low frequencies. Because a straight line leads to a very inefficient use of the available chip area, the stripline is usually arranged in a meandering fashion. If the distance between neighboring segments is large enough the additional effects can be neglected. From that it follows that the area required scales with the inverse of the frequency. However, due to the space between the turns, this leads to a suboptimal use of the available area, which in turn has the consequence that low frequency CPW resonators get quite large.

2.2.2 Effective Permittivity

To accurately predict the fundamental frequency and higher modes of CPW resonators, it is sufficient to know the effective permittivity of the stripline (in addition to the length).

The effective permittivity of a single-layered unshielded stripline can be calculated analytically using conformal mapping techniques [6]

$$\varepsilon_{\text{eff}} = 1 + \frac{\varepsilon_1 - 1}{2} \frac{K(k_1)}{K(k_1')} \frac{K(k_0')}{K(k_0)}, \tag{2.9}$$

where ε_1 is the electrical permittivity of the substrate, $K(k)$ gives the complete elliptic integral of the first kind and the arguments are given by

$$k_0 = \frac{w}{w + 2s}, \tag{2.10}$$

$$k_1 = \frac{\sinh\left(\frac{\pi w}{4h}\right)}{\sinh\left(\frac{\pi(w+2s)}{4h}\right)} \tag{2.11}$$

and $k' = \sqrt{1 - k^2}$ for $k = k_0, k_1$. The geometrical parameters w, s and h are defined in figure 2.2. This also allows the calculation of the capacitance per unit length C_l, the inductance per unit length L_l (using the expression

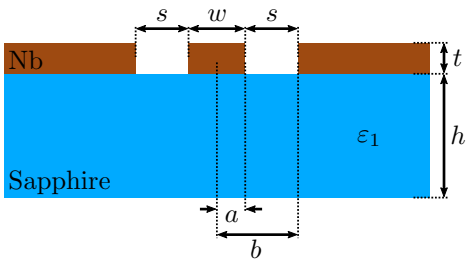

Figure 2.2: Cross section of the transmission line used in the CPW resonator. The niobium conductor (brown) of thickness t is on top the sapphire substrate of height h and electrical permittivity ε_1. The conductor has a width w and distance s to the ground plane on each side. The transmission line parameters a and b are related to the other parameters by $w = 2a$ and $s = b - a$.

$v_{\text{ph}} = 1/\sqrt{L_l C_l}$ [12]) and the characteristic impedance Z_0 [15]

$$C_l = 4\varepsilon_0 \varepsilon_{\text{eff}} \frac{K(k_0)}{K(k_0')}, \tag{2.12}$$

$$L_l = \frac{\varepsilon_{\text{eff}}}{c^2 C_l} = \frac{\mu_0}{4} \frac{K(k_0')}{K(k_0)}, \tag{2.13}$$

$$Z_0 = \sqrt{\frac{L_l}{C_l}} = \frac{1}{4}\sqrt{\frac{\mu_0}{\varepsilon_0 \varepsilon_{\text{eff}}}} \frac{K(k_0')}{K(k_0)}. \tag{2.14}$$

The parameters for the chips used in the experiments at QuDev were the following: $t = 150\,\text{nm}$, $h = 500\,\mu\text{m}$, $w = 10\,\mu\text{m}$ and $s = 4.5\,\mu\text{m}$. Given these dimensions, it is clear that $t \ll h$, and so the effective permittivity is approximated by the limit case $h \to \infty$. This results in a constant effective permittivity: For $h \to \infty$ it follows that $k_1 \to w/(w + 2s) = k_0$ and hence

$$\varepsilon_{\text{eff}} = \frac{1 + \varepsilon_1}{2}. \tag{2.15}$$

The substrate used for the fabricated chips is sapphire Al_2O_3 and the superconductor is niobium. The relative permittivity of sapphire is anisotropic with $\varepsilon_{xy} = 9.3$ and $\varepsilon_z = 11.3$ at $T = 20\,\text{K}$ [10]. Considering the weak temperature dependence right above $T = 20\,\text{K}$, one can assume that those values give reasonable estimates even for lower temperatures. Furthermore, it has to be assumed that the values are valid for frequencies in the range of several hundred megahertz even though the measurements of the effective permittivity were done in the range of 20 GHz.

For an anisotropic relative permittivity and height of a substrate an equivalent isotropic relative permittivity ε_{eq} and equivalent substrate height h_{eq} can be defined. They are given by [19] (for $\theta = 0$ and $\varepsilon_{xy} = \varepsilon_\perp$, $\varepsilon_z = \varepsilon_\parallel$):

$$\varepsilon_{\text{eq}} = \sqrt{\varepsilon_{xy}\varepsilon_z}, \quad h_{\text{eq}} = h\sqrt{\frac{\varepsilon_{xy}}{\varepsilon_z}} \tag{2.16}$$

Estimating the effective permittivity using equations (2.9) and (2.16) and the values given above, gives $\varepsilon_{\text{eff}} = 5.63$ compared to the value

$$\varepsilon_{\text{eff}} = 5.67, \tag{2.17}$$

which has previously been used for the design of CPW resonators with the same transmission line geometry and had been obtained from a Sonnet simulation. The calculated value deviates from the simulated value by less than 1%. Using the measured value for the effective permittivity and equations (2.12), (2.13) and (2.14) one obtains the numerical values $C_l = 1.58 \cdot 10^{-10}\,\mathrm{F\,m^{-1}}$, $L_l = 4.00 \cdot 10^{-7}\,\mathrm{H\,m^{-1}}$ and $Z_0 = 50.4\,\Omega$. To investigate the effect of gap width w, conductor width w on the effective permittivity and to decide whether they are relevant, each parameter was varied separately and the required length for a given fundamental frequency $f_0 = 500\,\mathrm{MHz}$ was calculated using equations (2.8), (2.9) and (2.16). The plots in figure 2.3 show that the influence is insignificant. For ease of fabrication and for simplicity s, w, h are therefore chosen to take the standard values, which allows the use of previously fitted values for $\varepsilon_{\mathrm{eff}}$.

2.2.3 Design Optimization

It has been shown in the previous section that there is only one significant free parameter of the one-dimensional geometry, the length l of the resonator; hence, the optimization in this respect is simple. Figure 2.5 shows the fundamental frequency as a function of length, as given by equation (2.8) for the effective permittivity (2.17). However, as mentioned before, the arrangement of the 1-D transmission line on the chip surface is highly relevant with respect to space efficiency. A meandering structure (as shown in figure 2.4) has proven very successful in the past and was therefore used as main geometry (an alternative geometry, the Hilbert curve, was considered in the mask design, see 3.1.1).

Given a certain rectangular bounding box described by $(\Delta x, \Delta y)$, the length of a meandering resonator with turning radius r filling that box is given by

$$l = 2N(l' + \pi r) + 2\left(\frac{l'}{2} + \pi r\right), \tag{2.18}$$

where $N = \left\lfloor \frac{\Delta x}{4r} \right\rfloor - 1$ is the number of meander turns and $l' = \Delta y - 2\left(r + \frac{w}{2} + s\right)$ the length of one straight segment. Figure 2.6 shows the fundamental frequency as achieved by filling the rectangle with a meandering CPW resonator according to equation (2.18).

2.2.4 Coupling and Quality Factor

Coplanar waveguide half-wavelength ($\lambda/2$) resonators are measured in transmission, hence they need to be coupled to the outside electronics on both ends (as shown in figure 2.4). For symmetric coupling, that is if both coupling capacitors have the same capacitance C_κ, then the coupled CPW resonator can be described in distributed element representation by the load R_L, the coupling capacitances C_κ, the resistance per length R_l, the inductance per length L_l, the capacitance to ground per length C_l and the length l [7]. Figure 2.7 shows the corresponding circuit diagram in distributed element representation. Inductance and capacitance per unit length can be calculated using equations (2.12) and (2.13).

When analyzing our measurements of these devices, the quality factors and coupling rates are of interest. The loaded quality factor Q_{L} in terms of induc-

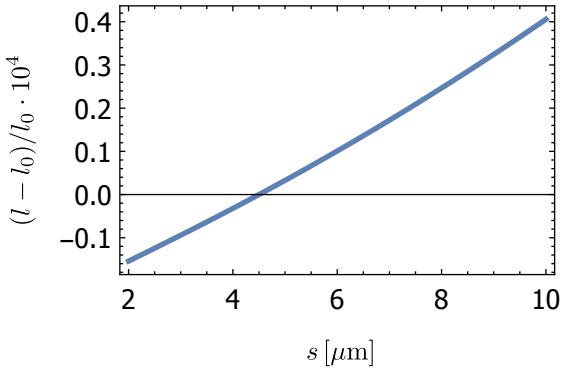

(a) Required length versus gap width s.

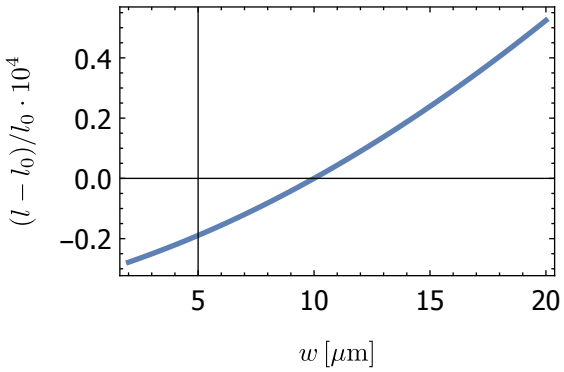

(b) Required length versus conductor width w.

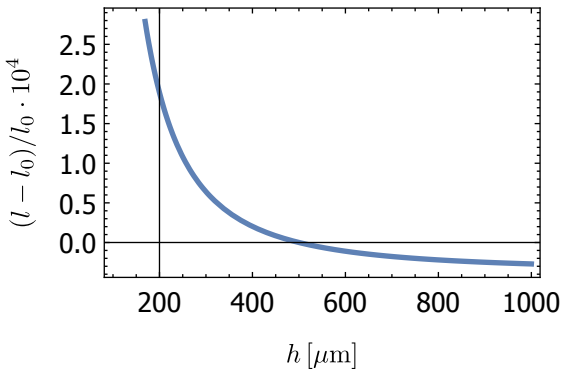

(c) Required length versus substrate height h.

Figure 2.3: Dependence of the required length l of a CPW resonator for a given frequency of $f_0 = 500\,\mathrm{MHz}$ as a function of (a) the gap width s, (b) the conductor width w and (c) the substrate height h. Shown is the relative difference from $l_0 = 126.400\,\mathrm{mm}$, which is obtained for the standard values ($s = 4.5\,\mu\mathrm{m}, w = 10\,\mu\mathrm{m}, h = 500\,\mu\mathrm{m}$). One can conclude that these parameters have negligible influence on the length.

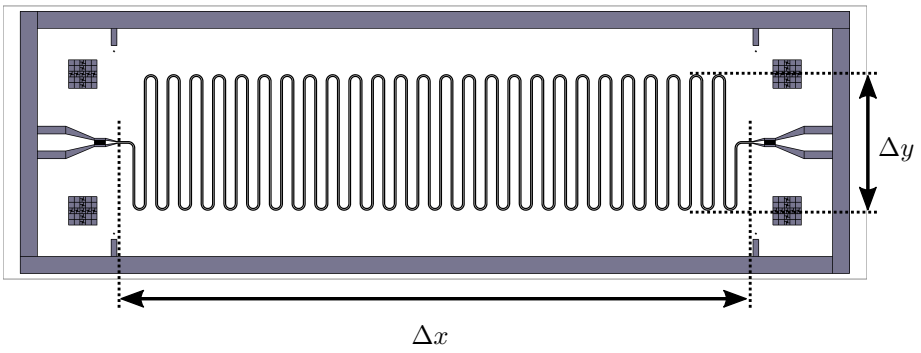

Figure 2.4: Meandering CPW resonator with both ends capacitively coupled. The conductor is shown in white and the sapphire substrate in dark blue.

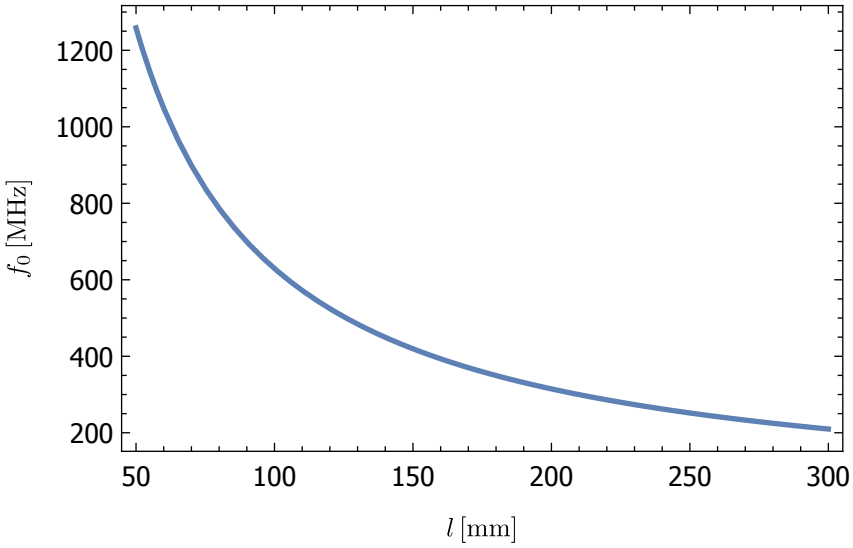

Figure 2.5: Fundamental frequency f_0 of a coplanar waveguide resonator as a function of the resonator length. The effective permittivity $\varepsilon_{\text{eff}} = 5.67$ was taken from a previous Sonnet simulation but agrees with the theoretical prediction within of less than 1%.

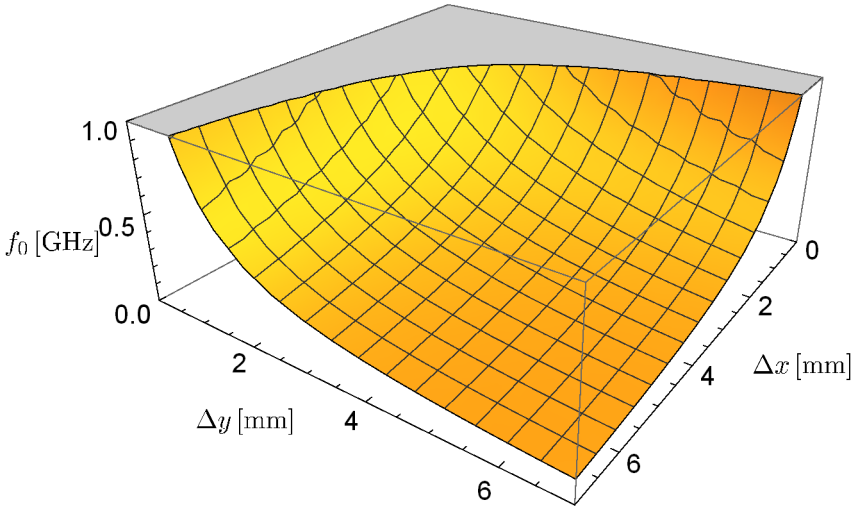

Figure 2.6: Considering a rectangular area with sides Δx and Δy, a CPW resonator in rectangular meander arrangement with turning radius $r = 50\,\mu$m (for the rounded meander turns) filling that area. Frequencies well below 500 MHz can be achieved.

tances and capacitances is given in [7] by the relations

$$Q_{\mathrm{L}} = \frac{Q_{\mathrm{int}} Q_{\mathrm{ext}}}{Q_{\mathrm{int}} + Q_{\mathrm{ext}}}, \tag{2.19a}$$

$$Q_{\mathrm{int}} = n\omega_0 \frac{C_l Z_0}{2\alpha} = n\omega_0 \gamma^{-1}, \tag{2.19b}$$

$$\begin{aligned} Q_{\mathrm{ext}} = \frac{n\omega_0 R^* C}{2} &= \frac{n\omega_0 C}{2}\left(\frac{1 + (n\omega_0 C_\kappa R_L)^2}{n^2\omega_0^2 C_\kappa^2 R_L}\right) \\ &= \frac{C}{2n\omega_0 C_\kappa^2 R_L}\left(1 + (n\omega_0 C_\kappa R_L)^2\right). \end{aligned} \tag{2.19c}$$

One can see Q_{int} is linear in the resonance frequency $\omega_0 = 2\pi f_0$ and mode number n, scaled by capacitance per length C_l, the CPW characteristic impedance Z_0, and the attenuation constant of the CPW line α, all of which are geometrical or material parameters. Together, these constitute the internal energy decay rate γ as given in equation (2.19b). The external quality factor Q_{ext} is governed by the total line capacitance $C = C_l l/2$, the coupling capacitance C_κ and the impedance of the feed line R_L. The coupling rate, defined in equation (2.46), is simply the ratio of ω_0 and Q_{ext}. This model is used in section 5.2.2 to characterize the CPW resonators.

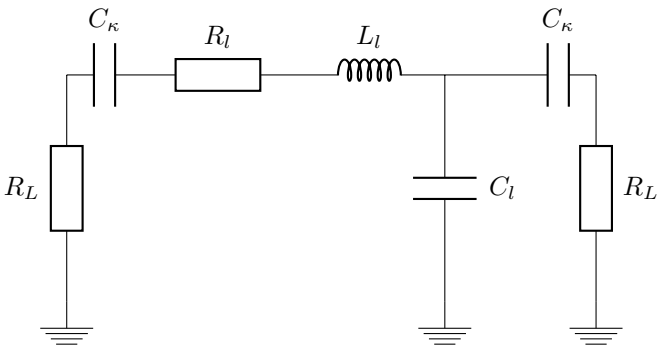

Figure 2.7: Distributed element representation of a symmetrically coupled transmission line resonator. The resistance, inductance and capacitance per length are denoted by R_l, L_l, C_l, the coupling capacitance by C_κ and the load by R_L.

2.3 Lumped Element Resonators

2.3.1 Basic Circuit Elements

Lumped element resonators are circuits that can successfully be described by a lumped element model. In reality the electrical quantities in distributed elements are dependent on the position; the lumped element model approximates the circuit by separating the circuit into abstract discrete elements, which leads to the electrical quantities losing their dependence on position. In the case of a simple transmission line based resonator this means that the main inductance and capacitance can be assigned to different parts of the transmission line.

For given substrate, metallic layers and transmission line properties, the physical quantities relevant for the circuit are determined by the geometry. The resonance frequency of an LC resonator is given by (see section 2.1.1)

$$\omega_0 = \frac{1}{\sqrt{LC}}, \tag{2.20}$$

hence the relevant quantities are the inductance L and the capacitance C.

In reality inductive elements have a certain capacitance and capacitive elements a certain inductance; those effects are called *parasitics* and lead to corrections to the physical quantities: As shown in figures 2.9 and 2.11 the combination of original circuit element and parasitic element can be reinterpreted as just one circuit element with frequency-dependent *effective* inductance or capacitance, respectively. The effective circuit is equivalent to the original (figure 2.1) with L and C replaced by L_{eff} and C_{eff}; hence, the effective frequency is given by

$$\omega_0^* = \frac{1}{\sqrt{L_{\text{eff}} C_{\text{eff}}}}, \tag{2.21}$$

where the expressions for the effective capacitance and inductance $L_{\text{eff}}, C_{\text{eff}}$ are derived in the succeeding paragraphs.

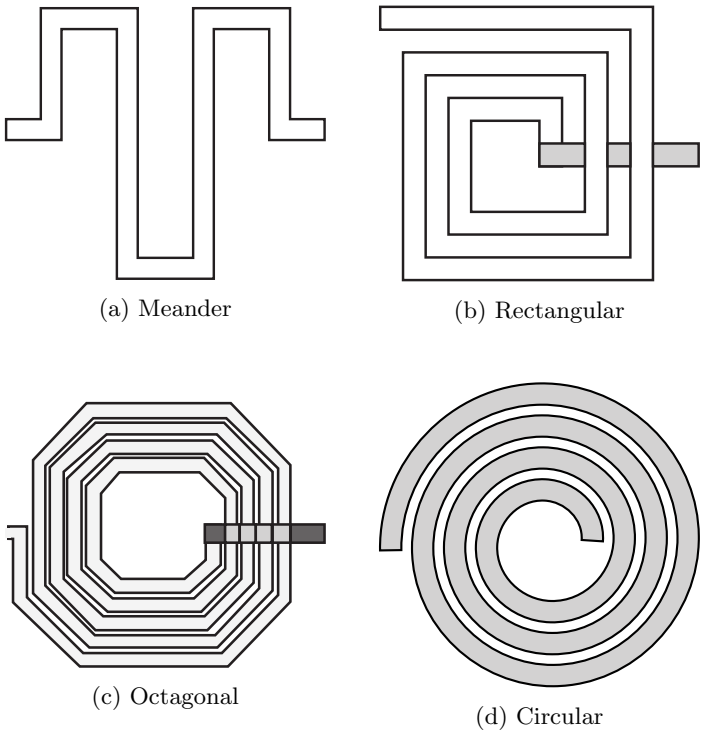

(a) Meander (b) Rectangular

(c) Octagonal (d) Circular

Figure 2.8: Two-dimensional inductor types [2]: (a) meander, (b) rectangular, (c) circular and (d) octagonal. Both, meander and rectangular configurations, have the advantage of an simple layout with the meander inductor additionally having a lower eddy current resistance; on the other hand they have low inductance and self resonance frequency. For the spiral resonators the more vertices there are (with circular counting as infinite) the more difficult the layout is and the higher the inductance and self resonance frequency [2].

Inductance

There are several realizations of two dimensional planar inductors, including a small section of a strip conductor, circular or rectangular loops, circular or rectangular spirals and meander inductors [2]. Meander inductors are easy to design and fabricate.

For inductor configuration both the self-inductance of the single conductive segments, which describe the effect of an induced voltage by the changing current, as well as the mutual inductance of two segments in proximity, which induce voltages in each other, have to be considered. The mutual inductance depends strongly on the geometrical arrangement.

As mentioned above, the effective inductance can be modeled as a parasitic capacitance in parallel to the inductance. The parasitic capacitance comes from the capacitance between segments but also between each segment and the ground. By considering the total impedance of the equivalent circuit shown in

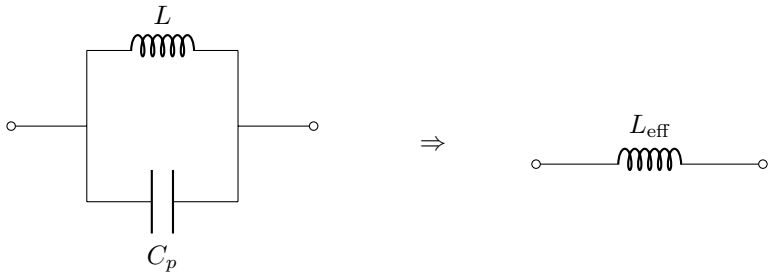

Figure 2.9: Equivalent circuit of an inductive element with inductance L and parallel parasitic capacitance C_p. By calculating the total impedance of this circuit the effective inductance L_{eff} can be determined.

figure 2.9 one finds [2]

$$\begin{aligned} i\omega L_{\text{eff}} = Z_{\text{ind}} &= \left(\frac{1}{Z_L} + \frac{1}{Z_C}\right)^{-1} = \left(\frac{1}{i\omega L} + i\omega C_p\right)^{-1} \\ &= \frac{i\omega L}{1-\omega^2 L C_p} = \frac{i\omega L}{1-(\omega/\omega_p)^2} \end{aligned} \tag{2.22}$$

with the self resonance frequency of the inductor $\omega_p := 1/\sqrt{LC_p}$, which results in the effective inductance

$$L_{\text{eff}} = \frac{L}{1-(\omega/\omega_p)^2}. \tag{2.23}$$

Capacitance

For capacitors there are basically three categories: microstrip, interdigital and *metal-insulator-metal* (MIM) capacitors (see figure 2.10). Microstrip capacitors are just segments of open-circuited microstrip sections, whereas interdigital capacitors utilize the capacitance between the *fingers* to increase the capacitance. In contrast to the other two categories, MIM capacitors require a multilevel process for fabrication [2]. Interdigital capacitors have proven to be a good candidate due to the simple fabrication and still relatively high achievable capacitance.

Similar to the case of inductors, interdigital capacitors have a small parasitic inductance due to finite length of the fingers. This can be modeled as effective capacitance, considering a parasitic inductance in series to the capacitance (figure 2.11 shows the equivalent circuit), which is due to the inductance of the conducting segments [2]

$$\begin{aligned} \frac{1}{i\omega C_{\text{eff}}} = Z_{\text{cap}} = Z_C + Z_L &= \frac{1}{i\omega C} + i\omega L_p \\ &= \frac{1-\omega^2 C L_p}{i\omega C} = \frac{1-(\omega/\omega_p)^2}{i\omega C} \end{aligned} \tag{2.24}$$

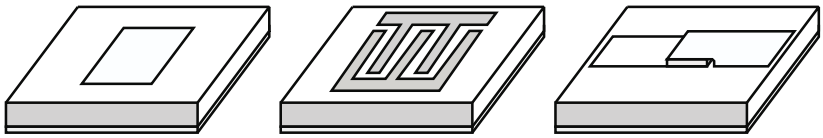

(a) Microstrip (b) Interdigital (c) MIM

Figure 2.10: Three categories of monolithic capacitors [2]. They differ in ease of fabrication and achievable capacitance value per unit area: (a) A single open-circuited microstrip section provides low capacitance. (b) Interdigital capacitors provide intermediate capacitance combined with easy fabrication. (c) MIM (metal-insulator-metal) capacitors require a multilevel fabrication process but give high capacitance per area.

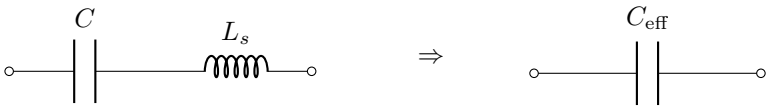

Figure 2.11: Equivalent circuit of a capacitive element with capacitance C and series parasitic inductance L_s. By calculating the total impedance of this circuit the effective capacitance C_{eff} can be determined.

with the self resonance frequency of the capacitor $\omega_s = 1/\sqrt{L_p C}$, which gives the effective capacitance as

$$C_{\text{eff}} = \frac{C}{1 - (\omega/\omega_s)^2}. \tag{2.25}$$

2.3.2 Meander Inductor

Stojanović et al. investigated different expressions for the calculation of inductance of meander inductors [16]. For optimal performance in optimization processes they generated a great number of values using analytical models and used fitting techniques to obtain an expression for the total inductance of a meander inductor in monomial form:

$$L_{\text{mon}} = 0.00266 \cdot a^{0.0603} \cdot h^{0.4429} \cdot N^{0.954} \cdot d^{0.606} \cdot w^{-0.173}, \tag{2.26}$$

where N is the number of long segments, the meaning of the layout dimensions a, h, d, w, which are given in μm, are defined in figure 2.12, and L_{mon} is given in nH. According to their investigation this expression gives maximally up to 12 percent relative error and also agrees with previously measured values.

The area taken up by the inductor is trivially given by

$$A_L = (2a + (n+1)d)(w+h), \tag{2.27}$$

where the meaning of the parameters can be seen in figure 2.12.

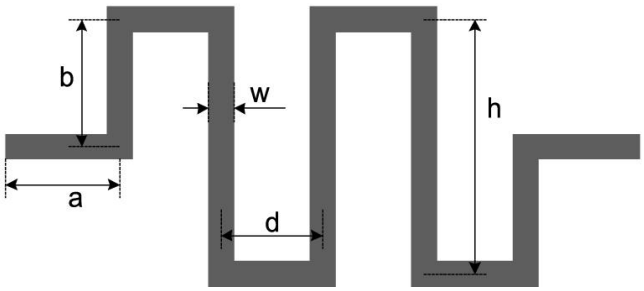

Figure 2.12: Meander inductor with layout dimensions a, h, d, w for $N = 3$. The conductor is shown in black, insulator in white [16].

2.3.3 Interdigital Capacitor

To estimate the capacitance of interdigital capacitors, two methods were used: a simple scaling relation based on parallel plate capacitors as well as a more elaborate expression that takes into account the microstrip structure. Figure 2.13 shows a schematic of such an interdigital capacitor with the relevant dimensions. For the simple scaling relation the capacitor is approximated as a parallel plate capacitor whose capacitance is given by

$$C = \frac{\varepsilon A}{d} \propto \frac{l}{d}, \tag{2.28}$$

where ε is the permittivity, $A = l \cdot t$ the area of the plates of dimensions l, t and d the separation between the plates; if there are N fingers, the number of *parallel plate capacitors* with dimensions l, t is $(N-1)$, hence

$$C \approx 10\,\mathrm{fF} \cdot (N-1)\frac{l}{200\,\mu\mathrm{m}}\frac{3\mu m}{d} = (N-1)\frac{l}{d} \cdot 0.15\,\mathrm{fF}, \tag{2.29}$$

where the constant $10\,\mathrm{fF}$ was determined by fitting the capacitance, obtained from simulations using the *Maxwell* software, as a function of N for constant $l = 200\,\mu\mathrm{m}$ and $d = 3\,\mu\mathrm{m}$.

A general expression for the total series capacitance of an interdigital capacitor is given by [2]

$$C = \frac{\varepsilon_{\mathrm{eff}}}{18\pi}\frac{K(k)}{K(k')}(N-1)l, \tag{2.30}$$

where K is the complete elliptic integral of the first kind with argument

$$k = \tan^2\left(\frac{\pi w}{4(w+d)}\right), \quad k' = \sqrt{1-k^2} \tag{2.31}$$

and the effective permittivity of the microstrip of width w on a substrate of height h is given by [2]

$$\varepsilon_{\mathrm{eff}} = \frac{\varepsilon_1 + 1}{2} + \frac{\varepsilon_1 - 1}{2}\left(\frac{1}{\sqrt{1+12\frac{h}{w}}} + 0.041\left(1-\frac{w}{h}\right)^2\right) \tag{2.32}$$

for $w \leq h$ with accuracy better than 1%. This reproduces the same dependence on N and l as in the simple scaling relation.

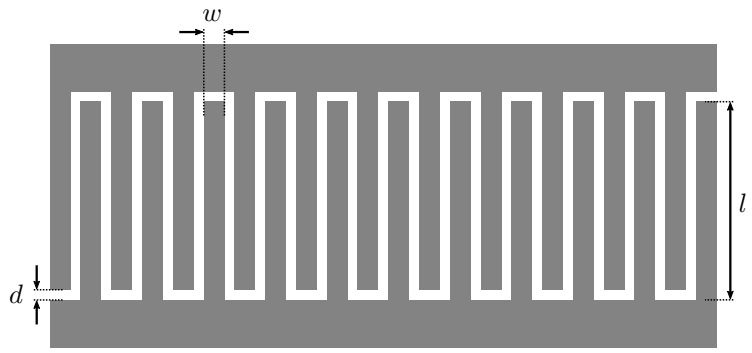

Figure 2.13: Schematic representation of an interdigital capacitor (*finger capacitor*) and the relevant dimensions: length of one finger l, separation of fingers d, width of a finger w as well as the number of fingers N (counting fingers from both sides). The conductor is shown in grey, the insulator in white.

The area of the capacitor is trivially given by

$$A_C = (l + d)(wN + d(N - 1)). \tag{2.33}$$

2.3.4 Design Optimization

Before finding optimal design parameters some practical limitations, especially concerning fabrication have to be considered: All the structures should have a size of at least $3\,\mu$m, due to the resolution of the photolitography process (except for the height of the niobium layer, which still is 150 nm). This constrains the optimization.

An optimization of the inductance per area over the parameter space h, d, w (see figure 2.12) for different number of turns, for different given values of inductance and for a given area which is then filled up by the inductor yields the minimally allowed values, that is $h = 6\,\mu$m, $d = 6\,\mu$m and $w = 3\,\mu$m (this holds for arbitrary given number of turns, inductance or area). For those optimal values figure 2.14 shows the dependence of the inductance per area for given area. For large areas (and similarly for large values of inductance, if that is fixed) the density decreases just very slightly. The effect of the turn length h is rather large (see figure 2.15) and for $l \gtrapprox 3\,\mu$m the density decreases with increasing finger length.

The optimization of the capacitance per area over the parameter space l, d, w (see figure 2.13) for a given area which is then filled up by the capacitor yields the minimum allowed values $d = 3\,\mu$m and $w = 3\,\mu$m (independent of the given area). For constant w, d, h equation (2.30) gives $C \propto (N-1)l \approx Nl$ (for $N \ll 1$) and equation (2.33) $A_C \approx l(w + d)N \propto Nl$ (for $N \ll 1$ and $l \ll d$, where the latter is satisfied for the optimal values). The condition $N \ll 1$ is satisfied for large areas if l is fixed. It follows that the capacitance per area saturates for large area:

$$\frac{C}{A} \approx \frac{\varepsilon_{\text{eff}}}{18\pi} \frac{K(k)}{K(k')} \frac{1}{w + d} = \text{const.} \tag{2.34}$$

The optimal finger length is more interesting: The simultaneous optimization given above yields a strong dependence of the optimal finger length on the

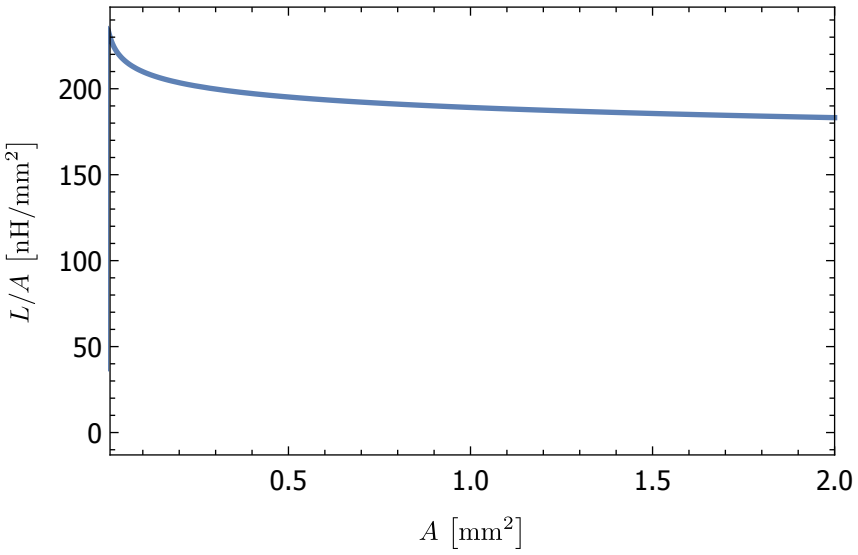

Figure 2.14: Inductance per area L/A of a meander inductor with optimal parameters $h = 6\,\mu$m, $d = 6\,\mu$m and $w = 3\,\mu$m (see figure 2.12) for given (a) area A or (b) inductance L. Both dependencies show a similar behavior: The density increases sharply for small values, then decreases first rapidly and then slowly.

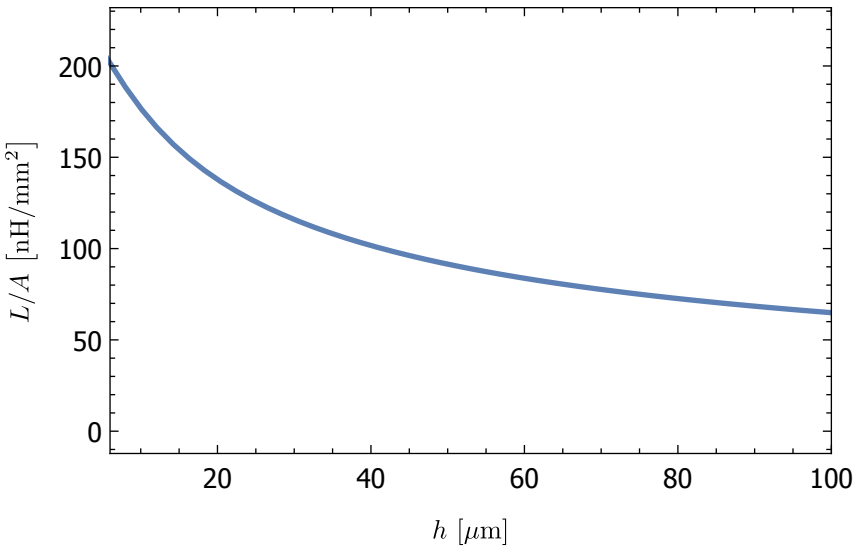

Figure 2.15: The inductance per area L/A of a meander inductor as a function of the length h of a meander turn. As expected, considering the result of the optimization, the density decreases with increasing length.

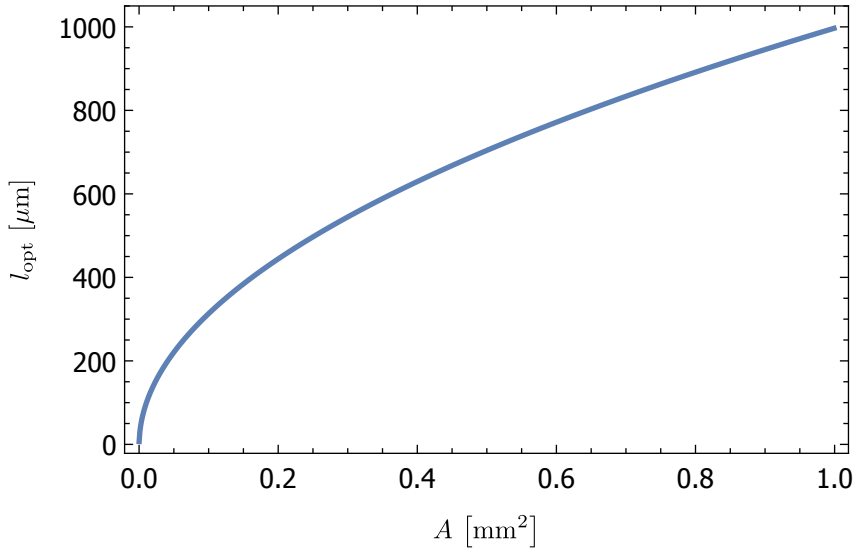

Figure 2.16: The simultaneous optimization of the capacitance per area for fixed area with respect to the parameters l, d, w results in a dependence of the optimal value for l on the area A.

given area (see figure 2.16), however considering the actual dependence as given by equation (2.34) it is obvious that even though small areas have a relevant optimum, for large areas the effect of the finger length on the capacitance density is negligible.

Because the dependence of the optimal inductance and capacitance density on the available area is insignificant for large areas, one can conclude that there is no clear preference for a specific division of the area between capacitor and inductor. The achievable resonance frequency f_0 as function of the inductor and capacitor area is shown in figure 2.17. The plot shows that on a total area of about $2\,\mathrm{mm}^2$ frequencies in the range of 200 MHz can be achieved. To check, the resonance frequency f_0 was also minimized directly over the whole parameter space $h_{\mathrm{ind}}, d_{\mathrm{ind}}, w_{\mathrm{ind}}, l_{\mathrm{cap}}, d_{\mathrm{cap}}, w_{\mathrm{cap}}$ for given inductor and capacitor area. The result was again independent of the actual value of the two areas and yielded, as expected, the minimum allowed value of $3\,\mu$m for h_{ind}, d_{ind}, w_{ind}, d_{cap} and w_{cap} (up to a numerical tolerance of 2%).

Because the simple scaling relation from equation (2.29) was fitted to data originating from capacitors with $d = w = 3\,\mu$m and because the dependence on l and N is the same as in the model described by equation (2.30), it can be used instead. This simplification allows faster computation and, due to the fitting of the parameter, has been shown to be consistent with the specific chip type and fabrication methods.

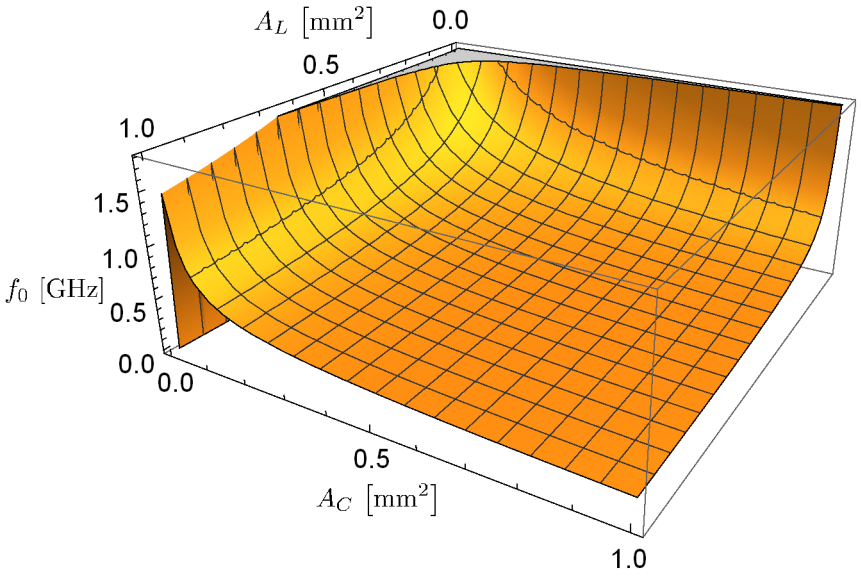

Figure 2.17: Achievable resonance frequency $f_0 = \frac{\omega_0}{2\pi}$ according to equation (2.20) as a function of the inductor area A_L and the capacitor area A_C for turn length $h_{\text{ind}} = 50\,\mu\text{m}$ and finger length $l = 500\,\mu\text{m}$. Those values were chosen for reasons of practicality.

2.3.5 Lumped Element Circuit Model

Unloaded RLC Oscillator

The basic circuit model of an LC oscillator is shown in figure 2.1. Losses can be modeled as a resistor in parallel (see figure 2.18). The voltage drops over the different elements are given by

$$V_R = RI_R, \quad V_L = L\dot{I}_L, \quad V_C = \frac{Q_C}{C} \tag{2.35}$$

and using Kirchhoff's voltage law for the left and right loop

$$V_R - V_L = 0, \qquad V_L - V_C = 0, \tag{2.36}$$

which gives $V := V_L = V_C = V_R$. Furthermore, $I_C = \dot{Q}_C$ and with Kirchhoff's current law

$$0 = I_R + I_L + I_C \tag{2.37}$$

or after differentiating once

$$0 = \dot{I}_R + \dot{I}_L + \dot{I}_C = \frac{\dot{V}}{R} + \frac{V}{L} + C\ddot{V}, \tag{2.38}$$

which can be rewritten as

$$\ddot{V} + \frac{\dot{V}}{RC} + \frac{V}{LC} = 0 = \ddot{V} + \gamma\dot{V} + \omega_0^2 V \tag{2.39}$$

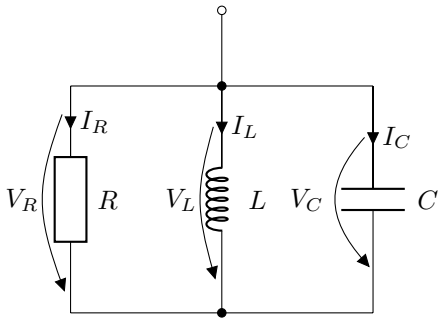

Figure 2.18: Circuit diagram of an RLC parallel oscillator with resistance R, inductance L and capacitance C.

with loss rate $\gamma := \frac{1}{RC}$ and the resonance frequency $\omega_0 = \frac{1}{\sqrt{LC}}$. Equation (2.39) is the equation of motion of a damped harmonic oscillator with resonance frequency ω_0.

Loaded RLC Oscillator

In order to allow reflection measurements, the resonator has to be coupled to the transmission line and outside electronics. In our case this can be done capacitively. Furthermore, the RLC circuit couples capacitively to the ground by the parasitic capacitance C_g, which is given by the insulating border between the circuit elements and the ground plane. There is also a parasitic capacitance $C_{g,p}$ to ground parallel to the resonator. Figure 2.19 shows the complete equivalent circuit.

From a geometrical perspective (see chapter 3) it can be expected that the values of the parasitic capacitances are much smaller than the capacitance C of the main capacitor, which then leads to a comparatively small and negligible frequency shift. In that range of values, an increase in C_g or $C_{g,p}$ are seen to have reduce the coupling. The effect on both the frequency and the coupling rate can be seen when analyzing the impedance of the circuit as a function of frequency and varying the parasitic capacitances. Matching the two capacitances to ground to actual geometrical features of the design (proposed in section 3.2.4 and shown in figure 3.7) shows that the parallel capacitance basically gives the capacitance of the island (the place where the coupling capacitor connects to both the main capacitor as well as the inductor) to ground. Due to the point-like character of the island, $C_{g,p}$ can be assumed to be much smaller than C_g. The parallel parasitic capacitance is therefore neglected in the following analytic analysis, however it should be stressed that its qualitative effect in the considered range of values is the same as the one of the series capacitance.

When neglecting $C_{g,p}$ as justified above, the total impedance of that circuit

is given by

$$Z(\omega) = \underbrace{Z_{\text{load}}}_{=R_L} + \underbrace{Z_\kappa}_{=\frac{1}{i\omega C_\kappa}} + \underbrace{\left(\frac{1}{Z_L} + \frac{1}{Z_C} + \frac{1}{R}\right)^{-1}}_{=\frac{i\omega L}{1-(\omega/\omega_0)^2+i\omega L/R}} + \underbrace{Z_g}_{=\frac{1}{i\omega C_g}} \tag{2.40}$$

$$= \frac{i\omega L}{1-(\omega/\omega_0)^2 + i\omega L/R} + \frac{(C_g + C_\kappa)}{i\omega C_g C_\kappa} + R_L. \tag{2.41}$$

This can be rewritten as

$$Z(\omega) = \frac{i\omega L}{1-(\omega/\omega_0)^2 + i\omega L/R} + \frac{1}{i\omega \tilde{C}_\kappa} + R_L \tag{2.42}$$

with

$$\tilde{C}_\kappa = \frac{C_g C_\kappa}{C_g + C_\kappa}. \tag{2.43}$$

The effective circuit is shown in figure 2.20. In the overcoupled case ($R \to \infty$) this allows the calculation of the coupling rate via an equivalent circuit as shown in figure 2.18 and the corresponding equation of motion according to [3] (in the approximation $\tilde{C}_\kappa \ll C$, which is satisfied for the assumptions described above)

$$\kappa \approx \frac{\tilde{C}_\kappa{}^2 R_L}{C^2 L}. \tag{2.44}$$

For the design process, however, no capacitance to ground has been accounted for, hence

$$\kappa^{\text{designed}} \approx \frac{C_\kappa^2 R_L}{C^2 L}. \tag{2.45}$$

From that the external quality factor, which describes the interaction with the load, can be calculated:

$$Q_{\text{ext}} = \frac{\omega_0}{\kappa} = \frac{2\pi f_0}{\kappa}. \tag{2.46}$$

The undercoupled case ($C_\kappa \to \infty$) allows the calculation of the internal loss as given above

$$\gamma = \frac{1}{RC} \tag{2.47}$$

and the internal quality factor

$$Q_{\text{int}} = \frac{\omega_0}{\gamma} = \frac{2\pi f_0}{\gamma}. \tag{2.48}$$

If the two loss rates γ and κ are comparable, the resonator is usually said to be *critically coupled*.

2.4 Microwave Network Analysis

This section summarizes the basics concerning microwave network analysis as used later in this work. A more in-depth introduction to this topic is given for example in [12].

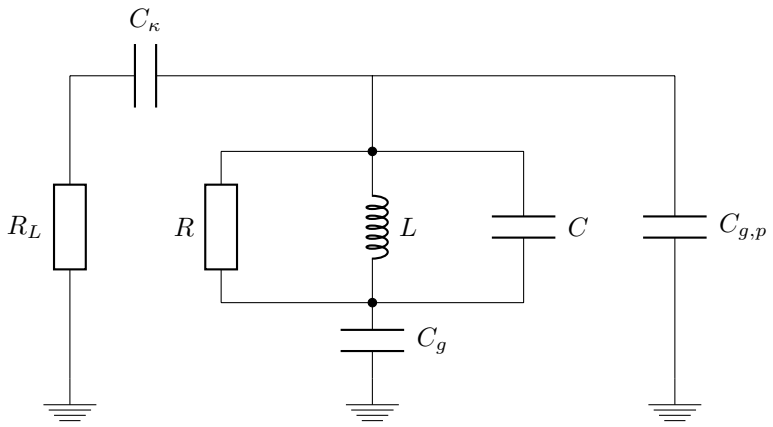

Figure 2.19: Lumped element circuit diagram for a loaded RLC parallel resonator. The inductance L and capacitance C make up the main part of the resonator, losses are modelled by the resistance R and the resonator is capacitively coupled to the load R_L via the capacitance C_κ. Additionally, the RLC circuit part couples capacitively to the ground by the parasitic capacitances C_g and $C_{g,p}$.

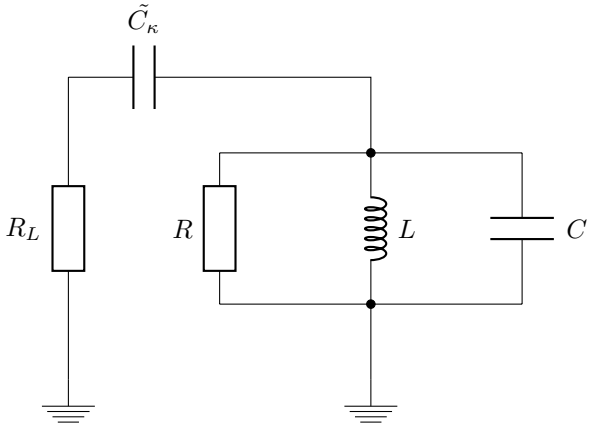

Figure 2.20: Simplified lumped element circuit diagram for a loaded RLC parallel resonator. The inductance L and capacitance C make up the main part of the resonator, losses are modelled by the resistance R and the resonator is capacitively coupled to the load R_L via the effective capacitance $\tilde{C}_\kappa$ which accounts for the capacitative coupling to ground shown in figure 2.19 in the case of $C_{g,p} \to 0$.

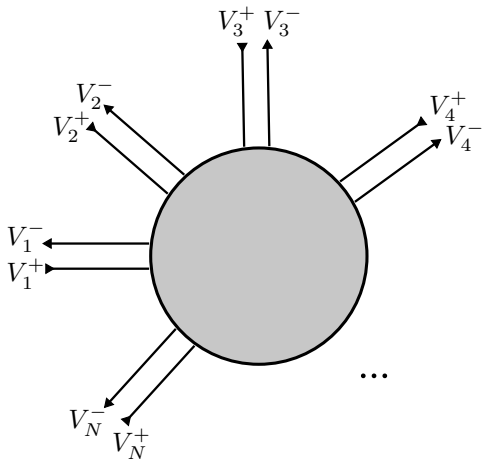

Figure 2.21: Multiport network. Each port gives an input signal with amplitude V_n^+ and an output signal with amplitude V_n^-.

2.4.1 Multiport Network

A multiport, more specific an N-port, microwave network is characterized by N ports numbered by $n = 1, 2, \ldots, N$ and each port gives an input signal with amplitude V_n^+ and an output signal with amplitude V_n^- (see figure 2.21). The total voltage at each port is therefore given by $V_n = V_n^+ + V_n^-$. Analogously we can define the input I_n^+ and output I_n^- as well as total current $I_n = I_n^+ - I_n^-$ at each port.

The voltage and current amplitudes are related to each other by the internal structure of the network. In terms of just input and output signals this relation is described by the impedance matrix, where each matrixelement is defined by

$$Z_{ij} = \left.\frac{V_i}{I_j}\right|_{I_k=0 \text{ for } k\neq j}, \tag{2.49}$$

and hence

$$\begin{pmatrix} V_1 \\ V_2 \\ \vdots \\ V_N \end{pmatrix} = \underbrace{\begin{pmatrix} Z_{11} & Z_{12} & \cdots & Z_{1N} \\ Z_{21} & Z_{22} & \cdots & Z_{2N} \\ \vdots & \vdots & \ddots & \vdots \\ Z_{N1} & Z_{N2} & \cdots & Z_{NN} \end{pmatrix}}_{=Z} \begin{pmatrix} I_1 \\ I_2 \\ \vdots \\ I_N \end{pmatrix}. \tag{2.50}$$

2.4.2 Scattering Matrix

The scattering matrix gives a complete description of the network in terms of input and output at its N ports. In matrix notation it can be defined by

$$\begin{pmatrix} V_1^- \\ V_2^- \\ \vdots \\ V_N^- \end{pmatrix} = \underbrace{\begin{pmatrix} S_{11} & S_{12} & \cdots & S_{1N} \\ S_{21} & S_{22} & \cdots & S_{2N} \\ \vdots & \vdots & \ddots & \vdots \\ S_{N1} & S_{N2} & \cdots & S_{NN} \end{pmatrix}}_{=S} \begin{pmatrix} V_1^+ \\ V_2^+ \\ \vdots \\ V_N^+ \end{pmatrix}. \tag{2.51}$$

A single matrix element is therefore given by

$$S_{ij} = \left.\frac{V_i^-}{V_j^+}\right|_{V_k^+=0 \text{ for } k\neq j}, \tag{2.52}$$

which also gives the measuring instruction of that matrix element: S_{ij} is determined by driving only port j with input signal of amplitude V_j^+ and measuring the reflected signal amplitude V_i^- at port i.

The relation to the impedance matrix Z is given by [12]

$$S = (Z + \mathbb{1})^{-1}(Z - \mathbb{1}) \qquad \Leftrightarrow \qquad Z = (\mathbb{1} + S)(\mathbb{1} - S)^{-1}. \tag{2.53}$$

Chapter 3

Mask Design

This chapter gives an overview over the resonator designs that have been fabricated. The coplanar waveguide design is the standard meandering arrangement of a transmission line and has previously been studied. The design used for the lumped element resonators, however, has been newly developed and implemented on this scale. The different components of that design are discussed in more detail. The relevant parameters and properties of the resonators that have been fabricated are summarized in section 3.3.

3.1 Coplanar Waveguide Resonators

The design used for the coplanar waveguide resonators is shown in figure 2.4 and has already been used extensively [7, 15]. Using equation (2.18) the length of the resonator was calculated given the bounding box and turning radius. For the microstrip the standard parameters $a = 5\,\mu\text{m}$ and $b = 9.5\,\mu\text{m}$, which yield $w = 10\,\mu\text{m}$ and $s = 4.5\,\mu\text{m}$ (see figure 2.2), have been used.

3.1.1 Hilbert Curve Geometry

The Hilbert curve is a space-filling curve whose length grows exponentially with the order of the curve while being bounded by the same rectangle. Figure 3.1 shows a CPW resonator on a size 1 chip with Hilbert curve like arrangement of the transmission line instead of the usual meander arrangement.

3.1.2 Launchers and Coupling Capacitors

To allow for transmission measurements the coplanar waveguide resonator is coupled capacitively to the outside (cables) via two launchers (see figure 3.2 for the dimensions). In order to achieve a constant external Q-factor Q_{ext} the required coupling capacitance C_κ was determined for given L and C of the resonator and from that the required and optimal finger length l_c and number of fingers was estimated. Figure 3.3 shows a close-up of the interdigital coupling capacitor.

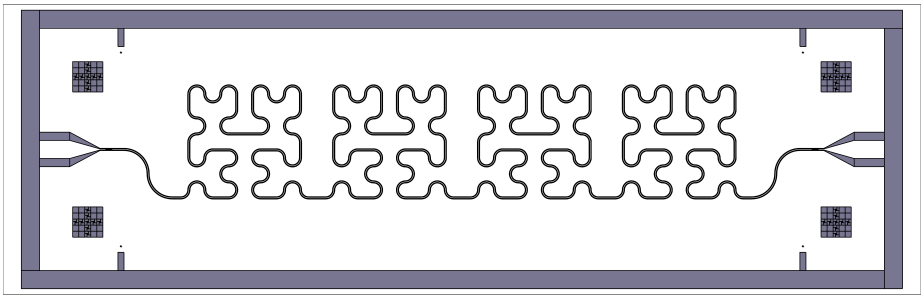

Figure 3.1: Hilbert curve geometry for a CPW resonator. This design results in a resonance frequency of $f_0 = 2.10\,\mathrm{GHz}$. The conductor is shown in white and the sapphire substrate in dark blue.

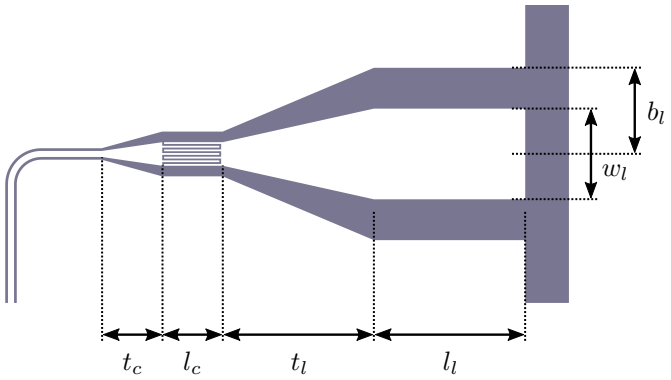

Figure 3.2: The launcher and coupling capacitor at one end of a CPW resonator. The width of the launcher was chosen $w_l = 150\,\mu\mathrm{m}$ while the ratio between conductor with and total width was kept the same as in the case of the tranmission line, that is $\frac{b_l}{a_l} = \frac{b}{a} = \frac{9.5}{5}$ with $a_l = w_l/2$. The length of the other pieces were as follows: launcher $l_l = 250\,\mu\mathrm{m}$, launcher taper $t_l = 250\,\mu\mathrm{m}$ and capacitor taper $t_c = 100\,\mu\mathrm{m}$. The gap size between the capacitor fingers was chosen to be $3\,\mu\mathrm{m}$. The conductor is shown in white.

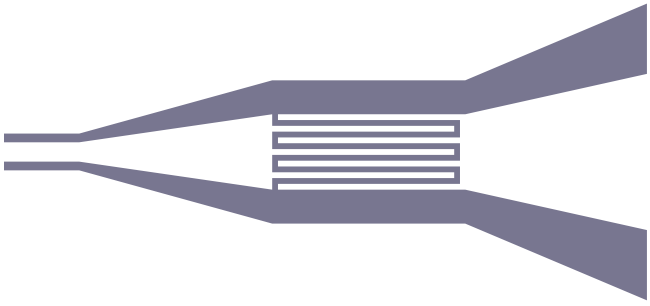

Figure 3.3: Coupling capacitor at one end of a CPW resonator; an interdigital capacitor is used. See figure 3.2 for the dimensions. The conductor is shown in white.

3.2 Lumped Element Resonators

For the lumped element resonators several different geometries were considered: different types of inductors and capacitors as well as different arrangements of them on a chip. Meander inductors and interdigital capacitors were chosen as basic elements of the new geometry. However, the established arrangement was impractical for achieving low frequencies due to not being very scalable. The main goals the new arrangement had to satisfy was efficient space usage on the chip (that is low achievable frequency for a given area) as well as being easily scalable. The latter requires a design that takes some input parameters and adapts to those.

3.2.1 Supermeander Inductor

In order to efficiently use the space on the chip with given aspect ratio, an additional level of meandering was introduced into the meander inductor: so called *superturns*, as shown in figure 3.4. This allows much longer inductors without needing very long and narrow chips. For consistency in the arrangement both ends of the inductor are on the same side; this however requires that there is a connecting straight line if the number of superturns is odd (see figure 3.4b).

The geometrical parameters for a single superturn are as shown in figure 2.12. In addition to that spacing parameters had to be introduced: the borders on top $B_\mathrm{t} = 10\,\mu\mathrm{m}$, bottom $B_\mathrm{b} = 10\,\mu\mathrm{m}$ and on the sides $B_\mathrm{s} = 20\,\mu\mathrm{m}$ as well as the (horizontal) separation between the superturns $S_\mathrm{st} = 10\,\mu\mathrm{m}$ and the line connecting two of them $S_\mathrm{s} = 10\,\mu\mathrm{m}$. Figure 3.4a shows those parameters on simple design examples.

In the design process the box size and geometrical parameters are given and from that the number of turns and superturns is calculated. The separation between the superturns is then adapted in order to achieve a symmetric structure, thereby adhering to the given minimal value.

3.2.2 Interdigital Capacitor

The design of the interdigital capacitor is as shown in figure 3.5 and described in section 2.3.3. Borders were added on top, bottom and on the sides on which the inductor is connected. The separation between capacitor and inductor was chosen to be $S_\mathrm{ci} = 10\,\mu\mathrm{m}$. The two connections (from both inducting parts) are on the same side in order to be able to easily connect the capacitor to the inductor (see section 3.2.4).

For given geometrical parameters the number of fingers is determined by the box height which is an input parameter for the design process as well.

3.2.3 Coupling Capacitor and Launcher

The lumped element resonator properties are determined by measuring the reflection coefficient, which requires coupling to the transmission line and outside electronics. Similarly to the case of the coplanar waveguide the launcher connects to an interdigital coupling capacitor (see figure 3.6). The launcher parameters were chosen according to the standard values used in the lab: $a_l = 75\,\mu\mathrm{m}$,

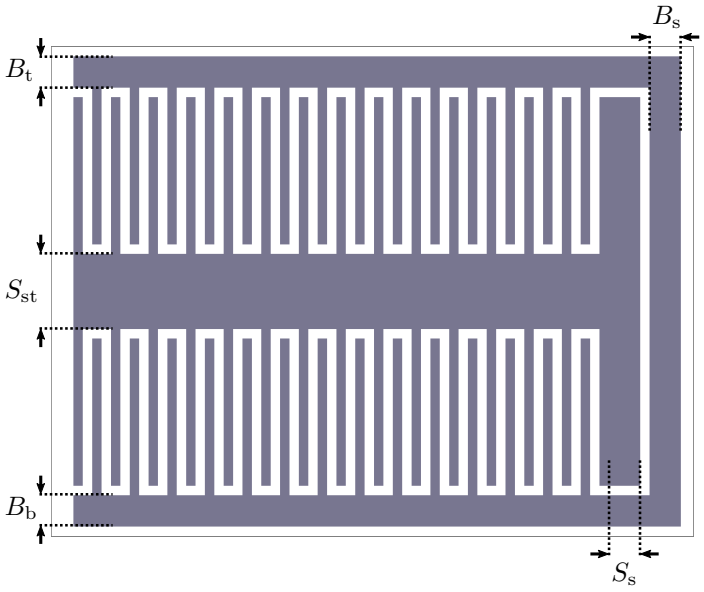

(a) Design for even number of superturns.

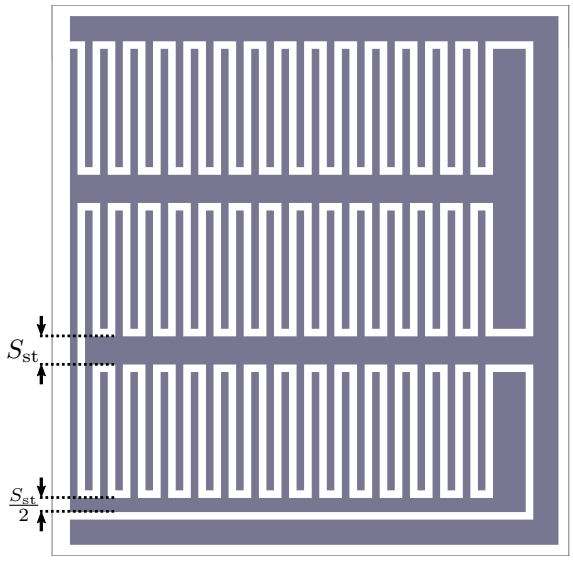

(b) Design for odd number of superturns.

Figure 3.4: The supermeander inductor combines traditional meander turns with additional turns of the whole structure, so called *superturns*. For the calculation of the inductance the mutual inductance between superturns is neglected, which is reasonable given the fairly large separation between them. For an even number of turns (a) the design is trivial, however for an odd number of turns (b) an additional conducting part has to be added in order to be able to consistently connect to the capacitor on the left hand side; this additional piece is ignored in the calculation of the inductance due to its negligible length compared to the length of the whole inductor. The conductor is shown in white and the sapphire substrate in dark blue.

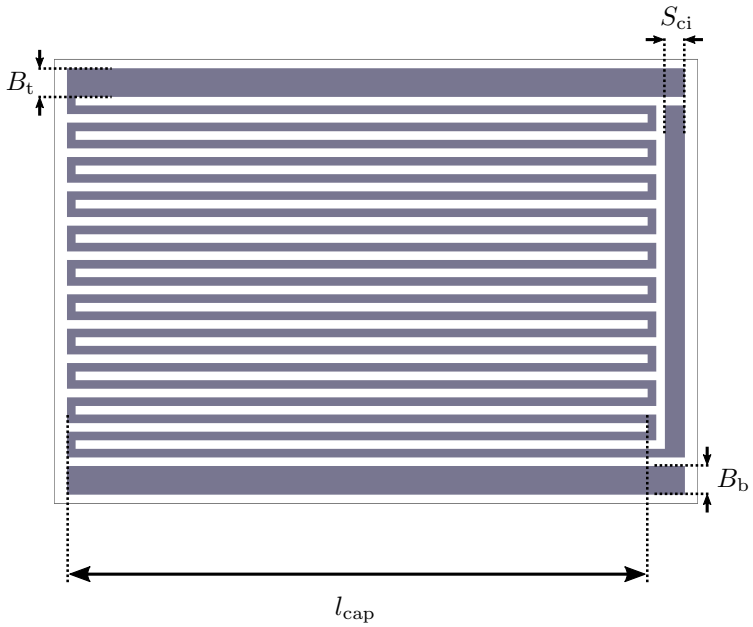

Figure 3.5: Interdigital capacitor used in the LE resonator. The finger and gap width were chosen to be $w_{\mathrm{cap}} = d_{\mathrm{cap}} = 3\,\mu\mathrm{m}$. The finger length is denoted by l_{cap}. The conductor is shown in white.

$a_l/b_l = 5/9.5$, launcher length $l_l = 250\,\mu\mathrm{m}$, launcher taper length $t_l = 250\,\mu\mathrm{m}$, distance between launcher and coupling capacitor $d_l = 200\,\mu\mathrm{m}$

3.2.4 Arrangement: Compact Resonator

The arrangement was inspired by the compact resonator design from [5]. Connecting the inductor directly to the capacitor is the most space efficient arrangement. Because both elements were designed such that the connections are on the same side, the connecting is straightforward. The equivalent lumped element circuit diagram is shown in figure 2.19.

For given geometrical parameters (conductor width w, meander inductor parameters $d_{\mathrm{ind}}, h_{\mathrm{ind}}$ (see figure 2.12), capacitor parameters l_{cap}, d_{cap} (see figure 2.13), border sizes and launcher configuration and a given box size $\Delta x, \Delta y$, first the capacitor is added such that it fills the box in y-direction (by calculating the number of fingers) and then the supermeander inductor such that it fills the remaining box (by choosing the number of turns and superturns).

3.3 Mask and Chips

In this section it is described what devices have been designed, why and how the geometrical parameters were determined from given physical ones. Three chip sizes were used; without subtracting the border widths their layout dimensions are: chip length $l_{\mathrm{chip}} = 7\,\mathrm{mm}$ and chip widths $w_{\mathrm{chip\ 1}} = 2\,\mathrm{mm}$, $w_{\mathrm{chip\ 2}} = 4.3\,\mathrm{mm}$, $w_{\mathrm{chip\ 3}} = 6.6\,\mathrm{mm}$.

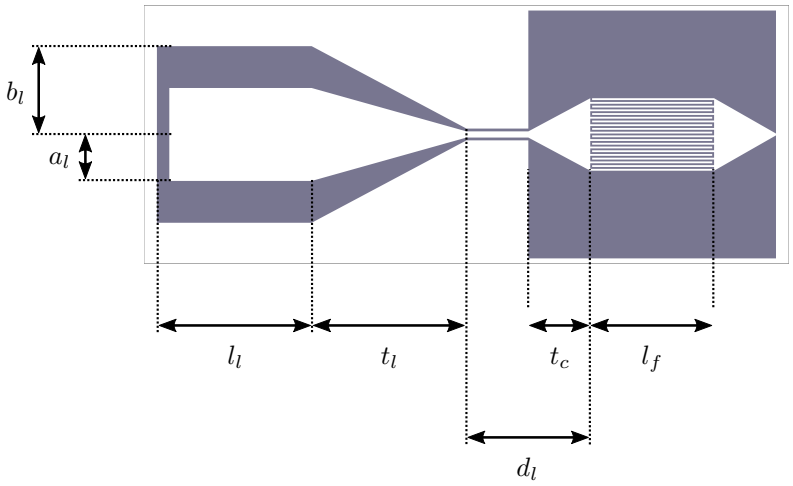

Figure 3.6: Launcher and coupling capacitor structure for lumped element resonators. The parameters are as follows: launcher transmission line dimensions (see figure 2.2) $a_l = 75\,\mu$m, $a_l/b_l = 5/9.5$, launcher length $l_l = 250\,\mu$m, launcher taper length $t_l = 250\,\mu$m, distance between launcher and coupling capacitor $d_l = 200\,\mu$m, coupling capacitor tapers length t_c and coupling capacitor finger length f_l. The conductor is shown in white.

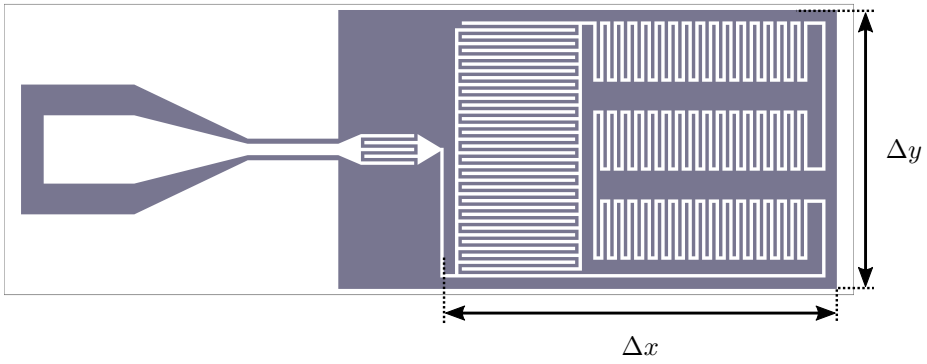

Figure 3.7: Pack arrangement for lumped element resonators consisting of a supermeander inductor and interdigital capacitor. Launcher, coupling capacitor, main capacitor and inductor are all packed closely, which allows efficient use of the available space. The conductor is shown in white.

3.3.1 CPW Resonators

For the CPW resonators three different studies were considered: variation of length, variation of turning radius and Hilbert curve geometry. See table 3.1. In the main study the length and therefore the frequency was varied while keeping all the other geometrical parameters constant. The designed fundamental frequencies range from 1.56 GHz down to 202 MHz. Because this design has already been well understood, the main goal was to investigate the behavior of those CPW resonators at low frequencies; this was done for the already established values for the other parameters, such as a, b and turning radius. For all the designs the external quality factor was chosen to be $Q_{\text{ext}} = 50000$. For a frequency of 3.02 GHz the turning radius was then varied from 50 μm to 150 μm and the Hilbert curve design was compared to a meander design of the same length and frequency.

Name	**Chip**	l **[mm]**	f_0 **[GHz]**	κ **[MHz]**	Q_{ext}	r **[μm]**
LFCPW01	1	40	1.56	0.0314	10000	50
LFCPW02	1	40	1.56	0.0314	10000	50
LFCPW03	1	65.775	0.951	0.0191	10000	50
LFCPW04	2	100	0.626	0.0126	10000	50
LFCPW05	2	187.675	0.333	0.0067	10000	50
LFCPW06	3	309.575	0.202	0.0041	10000	50
LFCPW07	1	20.754	3.02	0.0606	10000	150
LFCPW08	1	20.754	3.02	0.0606	10000	100
LFCPW09	1	20.754	3.02	0.0606	10000	50
LFCPW10	1	30	2.1	0.00761	275953	-
LFCPW11	1	30	2.1	0.21	10000	50

Table 3.1: Summary of all CPW designs that were fabricated. The parameters are: resonator length l, fundamental mode f_0, coupling κ, external quality factor Q_{ext} and turning radius r. The number in the column denotes the chip size as described at the beginning of section 3.3. The resonators 1 and 2 differ solely by the arrangement: 1 fills in x-direction, whereas 2 in y. (Note: Not all of those designs have been measured, see section 4.3.1.)

3.3.2 LE Resonators

The names and relevant parameters of all lumped element resonator designs are summarized in table 3.2. There are two studies: the variation of frequency (in the range 300 MHz to 6 GHz) and external quality factor (10^2 to 10^5) at fixed impedance $Z = 170\,\Omega$ and the variation of impedance (from 50 Ω to 300 Ω) at fixed frequency $f_0 = 3$ GHZ and for external quality factors of 10^3 to 10^5.

Due to the smaller size of the lumped element resonators two could be placed on each chip; usually a (large) low frequency resonator was paired with a (small) high frequency resonator to keep the distance between their ends as small as possible. Figure 3.8 shows an example of such an arrangement for the case of a 300 MHz and a 6 GHz resonator. Only size 1 chips were used.

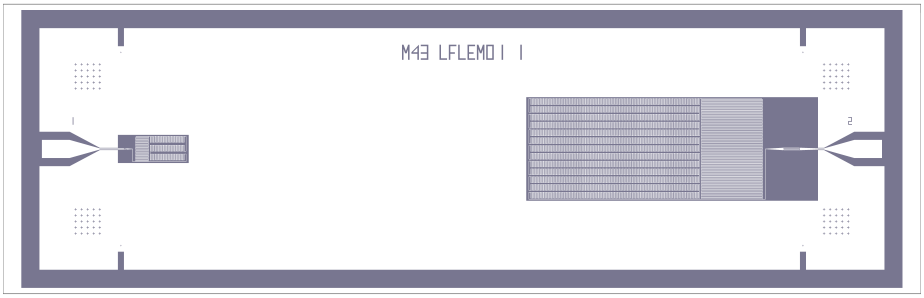

Figure 3.8: Example for the arrangement of two lumped element resonators on a size 1 chip (7 mm × 2 mm). At place 1 (left hand side) there is a 6 GHz resonator and at place 2 a 300 MHz. The conductor is shown in white and the sapphire substrate in dark blue.

Resonator Name	f_0 **[GHz]**	Q_{ext}	Z **[Ω]**	l_{cap} **[μm]**
LFLEM01_01	6	10^5	170	100
LFLEM02_02	6	10^4	170	100
LFLEM03_03	6	10^3	170	100
LFLEM04_04	6	10^2	170	100
LFLEM05_05	3	10^5	170	150
LFLEM06_06	3	10^4	170	150
LFLEM07_07	3	10^3	170	150
LFLEM08_08	3	10^2	170	150
LFLEM05_09	1	10^5	170	200
LFLEM06_10	1	10^4	170	200
LFLEM07_11	1	10^3	170	200
LFLEM08_12	1	10^2	170	200
LFLEM01_13	0.3	10^5	170	500
LFLEM02_14	0.3	10^4	170	500
LFLES01_14	0.3	10^4	170	500
LFLEM03_15	0.3	10^3	170	500
LFLEM04_16	0.3	10^2	170	500
LFLEM09_17	3	10^5	50	200
LFLEM09_18	3	10^5	100	150
LFLEM10_19	3	10^5	300	100
LFLEM10_20	3	10^4	50	200
LFLEM11_21	3	10^4	100	150
LFLEM11_22	3	10^4	300	100
LFLEM12_23	3	10^3	50	200
LFLEM12_24	3	10^3	100	150
LFLEM13_25	3	10^3	300	100
LFLEM13_26	3	10^4	400	100

Table 3.2: Summary of all LE designs that were fabricated. The designed resonance frequency is denoted by f_0, the external quality factor by Q_{ext}, the impedance by Z and the length of the fingers of the capacitor by l_{cap}. (Note: Not all of those designs have been measured, see section 4.3.1.)

Design According to Physical Parameters

In order to be able to design the resonators according to given physical parameters, that is with given frequency and impedance, instead of given geometrical parameters, estimation routines were implemented. For given frequency f_0, impedance Z and external quality factor Q_{ext} appropriate geometrical parameters have to be found for the layout. For that most of the geometrical parameters have to be previously specified; the box size $(\Delta x, \Delta y)$, the number of fingers in the capacitor, the number of turns and superturns of the inductor and the separation between superturns are determined from the given physical parameters. Additionally, a maximum box size and minimum separation between superturns have to be specified.

The main routine proceeds as follows:

1. Inductance L and capacitance C are determined from f_0 (equation (2.20)) and $Z = \sqrt{L/C}$.
2. Given the required value C the expression for the capacitance (equation (2.30)) is solved for the number of fingers N_{cap}.
3. The number of fingers N_{cap} determines the box height Δy.
4. The number of superturns N_{super} is found by filling the box in y-direction with superturns.
5. With the required inductance L the expression for the inductance (equation (2.26)) is solved for the number of turns N_{ind}, which then gives the box width Δx.
6. The separation between superturns is adapted from the minimum value in order to counter rounding effects and make sure that the inductor does fill the box in y-direction.

After that the coupling parameters have to be determined:

7. The expression for the external Q-factor is solved for the coupling capacitance C_κ (see equations (2.46) and (2.45)).
8. To determine the geometrical parameters that result in C_κ several different methods have been implemented (based again on equation (2.30)):
   (a) Solving for the number of fingers
   (b) Solving for the finger length
   (c) Solving for the the gap between the fingers
   (d) First solving for the number of fingers and then solving for the finger length in order to counter rounding effects (used for the fabricated designs)

3.4 Fabrication Process

The fabrication of the chips is done by photolitography; this requires a *mask* containing transparent and opaque areas for the structures. In order to fabricate

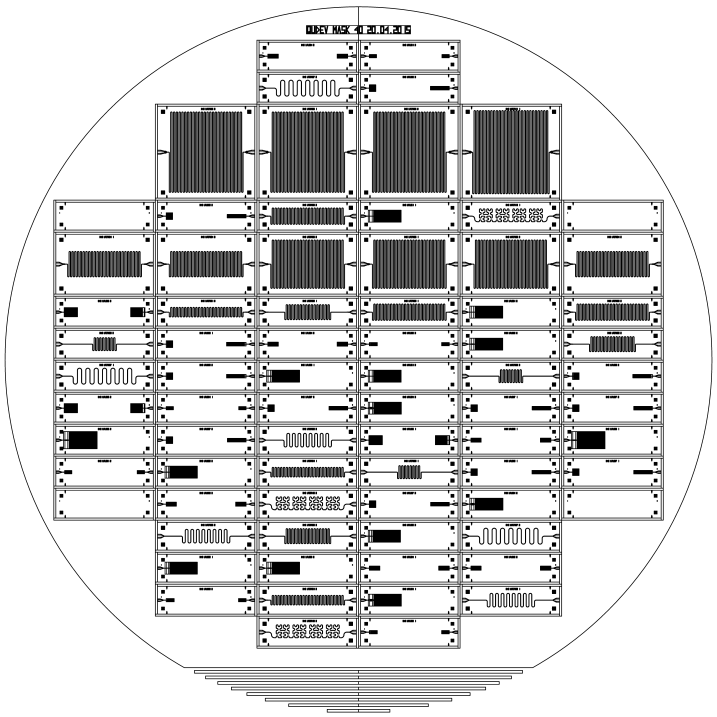

Figure 3.9: Digital graphics data showing all the chips with resonators on the wafer. The basic size of a chip is 2 mm × 7 mm and the sizes of the larger chips are chosen such that they match the height of 2 or 3 size 1 chips including a spacing of 300 μm for dicing. This results in the previously mentioned heights of 4.3 mm and 6.6 mm.

the mask digital graphics data describing it has to be produced. This is done with *Mathematica* which results in graphics data describing lines separating conducting from insulating parts. The graphics objects containing the data for each chip and the structures on it are joined and arranged on the (still digital) wafer (see figure 3.9). The data is then exported in the DXF file format which in turn is repaired (by joining open ends) and converted to the GDSII file format using the *LinkCAD* software.

The mask was produced at IBM and the photolitography done in the FIRST cleanroom at ETH Zurich. The basic steps of photolitography are the following (see figure 3.10): A resist is applied to the sapphire wafer of thickness 500 μm which is coated with a 150 nm thick layer of niobium (a), then the mask is pressed against it and exposed (b). The transparent areas in the mask allow exposure of the underlying areas on the wafer which results in the resist there becoming soluble. This is utilized and first the resist is removed (c) and then the niobium below etched away (d). The remaining resist is removed as well leaving the finished wafer with conducting niobium structures matching the opaque structures on the mask (e). In the last step the wafer has to be diced, that is cut, to produce single chips [15].

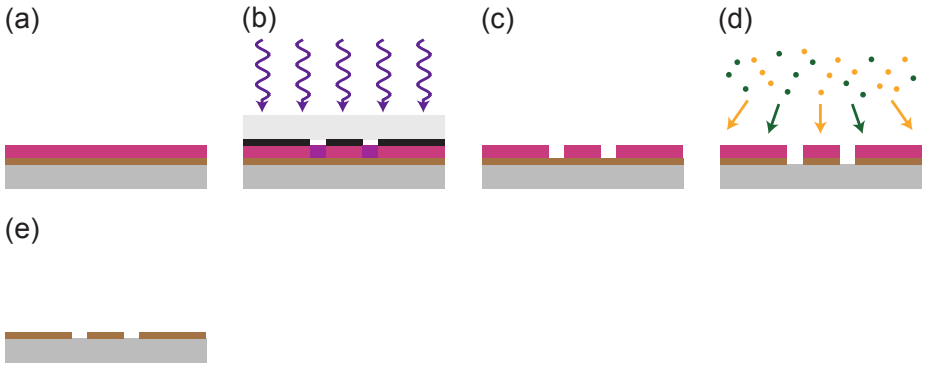

Figure 3.10: Fabrication of the wafer by photolitography [15]. The sapphire substrate is shown in grey, the niobium layer in brown and the resist in red. (a) Resist layer is applied. (b) Exposure. (c) Development. (d) Etching. (e) Resist stripping.

Chapter 4

Experiment

As described in sections 2.4 and 2.4.2 the resonators can be characterized by the scattering matrix measurements. In our experiment, we are interested primarily in reflection (transmission) coefficients for the lumped-element (coplanar waveguide) resonators. These parameters are measured directly using an Agilent N5230 vector network analyzer (VNA). To induce the superconducting state in our niobium-based ($T_c = 9.2$K) devices, the chips are immersed in a bath of liquid ^{4}He using a *dipstick*, a rigid assembly housing the microwave cables and supporting the sample. See figure 4.1 for a typical dipstick measurement setup at QuDev.

4.1 Sample Assembly

The microwave cabling running through the dipstick must be electrically connected to the resonators. The coaxial cable is connected to a coplanar waveguide on a copper-patterned printed circuit board (PCB) via an SMP launcher. The launchers are soldered to the PCBs using solder paste, a heat gun, toothpicks, and a thermally insulating work surface, such as a wooden plate. The solder paste is applied to the PCB ground and signal attachment sites, with great care taken not to create a short between them. The launchers are then placed onto the PCB, and heat is applied with the heat gun to activate the solder paste. Here, care must also be taken not to damage the copper by applying too much heat. This process is relatively quick when the PCB is isolated from thermally conductive materials. Each launcher-PCB connection must then be tested with a multimeter to verify the soldering was successful. See figure 4.2 to see an assembled sample.

Once the niobium-patterned sapphire chips are fabricated, they are wire-bonded to its corresponding PCB using the wire-bonder at FIRST. This process was not performed by the authors. See 4.3 for an example of wire bonds. Then, the samples are fastened to a copper base, and a copper PCB cover is placed over the sample (see figure 4.2) to prevent the chip from coupling to modes in the sample mount, and is fastened again. Then, after calibrating the vector network analyzer at the connection point of the sample ((c) in figure 4.1) using the Rosenberger SMP calibration kit (DUT: SMP Qudev, Male) ((d) in figure 4.1) the device is placed in the dipstick sample mount.

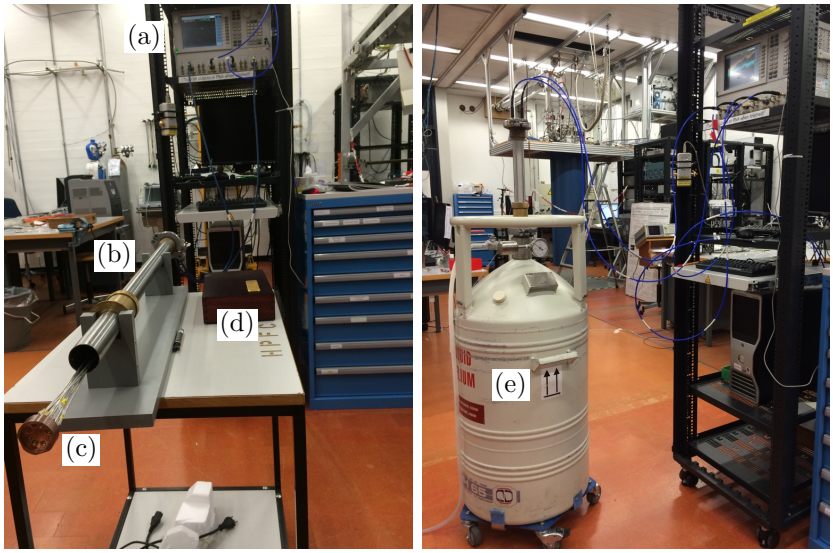

Figure 4.1: Main components of a dipstick measurement. (a) The VNA drives and measures the response of the load between any of its 4 ports (b) The dipstick (c) The sample box mount, where the coaxial cables connect to the launchers on the sample (d) The calibration kit used in the experiment (e) the ^{4}He dewar.

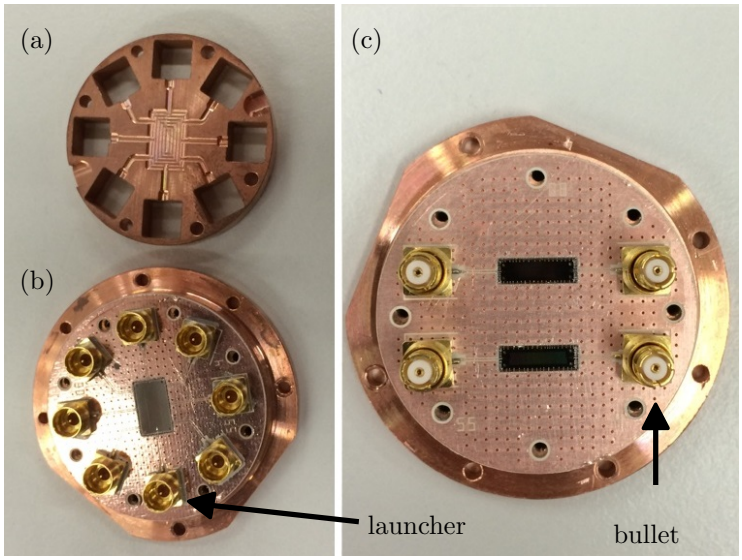

Figure 4.2: Images of samples in preparation for dipstick measurements. (a) PCB cover, shielding the resonator from spurious modes in the dipstick mount. (b) A "size 2" chip and PCB on the copper bottom plate of the dipstick mount. Only two of the launchers are connected to the chip. The launchers do not yet have bullets inserted. (c) Two "size 1" chips on a PCB, with bullets installed on the launchers. Note the shape of the bottom copper plate for orienting the sample.

4.2 Calibration

After choosing which VNA port corresponds to which PCB port (mapped via 4 of the 8 ports in the dipstick), the VNA must be calibrated. This is done using the short-open-load-reciprocal-thru (SOLR) method [9]. After choosing the desired IF bandwidth, number of points, input power, averaging factor and maximum frequency range, each port is measured with 3 standards and a through connection with one other port. Ideally, this calibration compensates for unwanted background spectra resulting from the cable setup, provided the calibration parameters are not changed.

For our experiment, the calibration of the VNA was done at the sample mount on the dipstick, rather than at the dipstick input port which connects to the VNA. This calibration is not experimentally ideal, because the thermal environment of the cables is not the same during experiment as during calibration. However, this is arguably closer than not calibrating the dipstick cables at all [13]. Naturally though, a background spectrum will be present in addition to the spectrum of the device under test (DUT) due to the change in attenuation constant of the cables. A way to distinguish between signal and background in reflection measurements that we performed was to measure after raising the dipstick so that the sample is slightly warmer. The change in resonance of the samples due to different kinetic inductance [13] allows one to view a frequency band without the resonance feature, while the background spectrum from the cables is largely unchanged. Then, we can renormalize the signal as compared to this measured background spectrum, enabling clearer characterization of the DUT. Background measurements were performed for the fundamental resonances of all lumped element devices. This is not useful with transmission measurements, as the signal-to-noise ratio is smaller, and so the thermal noise resulting from a change in bath temperature at a different dewar depth substantially alters the background spectrum.

4.3 Dipstick Measurement

With the sample in place, the helium dewar is prepared by connecting its boil-off line to the (open) recovery line and its level measured to be sure there is sufficient helium. Then, the neck is opened, and the dipstick is fastened to the neck via a KF flange. While we monitored the pressure gauge (a change of more than 0.3 bar is too high), the dipstick thermalized in the liquid helium, boiling off some into the recovery line. After a few minutes of slow submersion, much of the dipstick reached thermal equilibrium with the bath, and the dipstick was submerged more quickly without risk of too much pressure in the dewar. The dipstick is carefully submerged until the bottom is felt, at which point it is lifted slightly. It is important to place the dipstick in the dewar in a systematic way, such that we are confident the temperature of the sample is not too different between different trials.

Measurements of the sample via the VNA are straightforward. The samples with two "size 1" chips on the PCB form four-port microwave networks (figure 4.2), with 4 (2) resonators on two chips for the LE (CPW) devices. The CPW resonators on larger chips form two-port networks. Using the notation given by equation (2.52), the LE resonators were measured by probing S_{ii} with

the VNA port $1 \leq i \leq 4$, while the necessary transmission measurement S_{ij}, $1 \leq i, j \leq 4$ for CPW devices depends on how the VNA is connected to the dipstick input. One must then keep track of which VNA port corresponds to which port on the PCB, and then select the desired scattering matrix element to be recorded by the VNA. Typical parameters used in the experiment are an IF bandwidth of 50 kHz, 32000 points, −30 dBm power, and average factor of 20 and are kept constant after calibration.

4.3.1 Devices Measured

In total, seventy six devices were fabricated on Mask 43, with three duplicates of each unique device (and one with four, in fact). Of these, only about half of the 36 unique resonators were measured. However, from our measurements we can characterize both geometries as the fundamental resonance is decreased, and for the lumped-element model, as the impedance is varied. To study the device behavior with varying fundamental resonance, we measured (see tables 3.1 and 3.2 for associated parameters) devices LFCPW: 02, 03, 04, 05, and 06 for the coplanar geometry, and for the lumped element, LFLEM: 01_01, 01_13, 02_02, 02_14, 03_03, 03_15, 04_04, 04_16, 07_07, 07_11, 08_08, and 08_12. Additionally, devices LFLEM12_23, and LFLEM12_24 were measured. Two measured chips are pictured in figure 4.3.

4.3.2 Raw Spectra

Measuring the appropriate S-parameters over a broad spectrum is relevant for designing resonators and anticipating their properties. In particular, the presence of higher-order resonances is relevant to how effective these devices would be when coupled to other resonators and qubits. In this section, we present examples of raw measurements over the maximum calibrated frequency range provided by the VNA.

Coplanar-Waveguide Resonators

The coplanar waveguide resonators were measured in transmission. Though the behavior of CPW resonators is well-understood [7], QuDev has not fabricated CPW resonators at such low frequencies. The full-spectrum measurements (300 kHz to 18 GHz) follow the pattern of resonators with an inductive spectrum underneath. Note the point density is not as high in the fundamental resonance accompanying plot. This is not an issue, as point density can be lower for fitting transmission peaks. The details of fitting CPW transmission and LE reflection resonances is given in section 5.1.1.

Lumped Element Resonators

Measurements of the reflection coefficient for each resonator are carried out between 300 kHz and 18 GHz in segments of 4 GHz, resulting in a sampling interval of 0.125 MHz. Two examples of raw measurements from the VNA are shown in figures 4.6 and 4.7.

These data show a few higher-order modes for the 6 GHz resonator, as compared with the many modes present for the 300 MHz resonator. Further, it

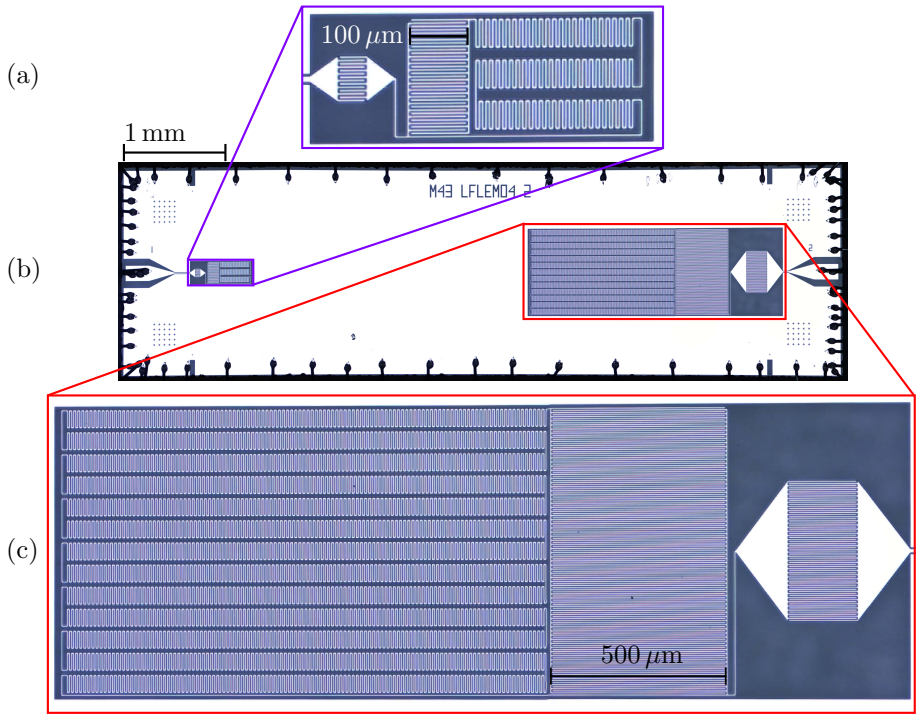

Figure 4.3: Image of a chip with two LE resonators. White is niobium, blue (gray) is sapphire. (a) The 6 GHz lumped-element resonator. (b) The "size 1" chip housing LFLEM_04 (left) and LFLEM_16 (right). Note the wire bonds connecting the chip to the PCB. (c) The 300 MHz resonator, at 1/20 of the fundamental resonance of (a), and 15 times the area.

.

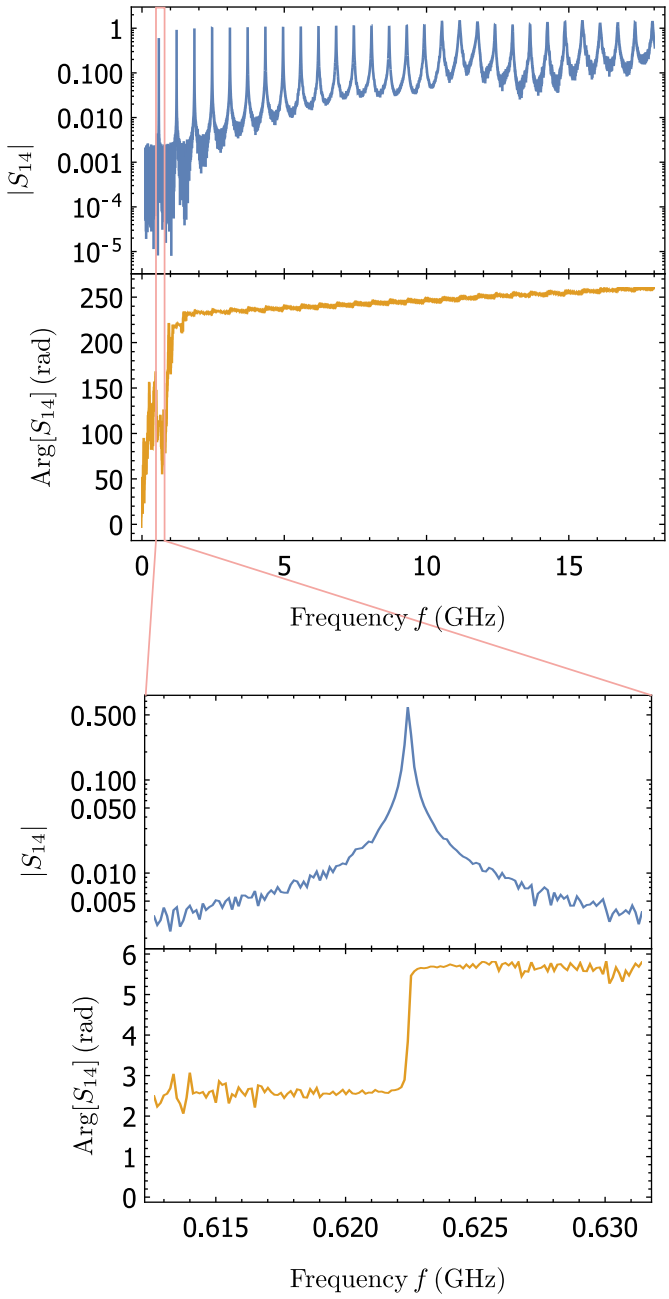

Figure 4.4: Transmission coefficient spectrum for CPW resonator LFCPW04.

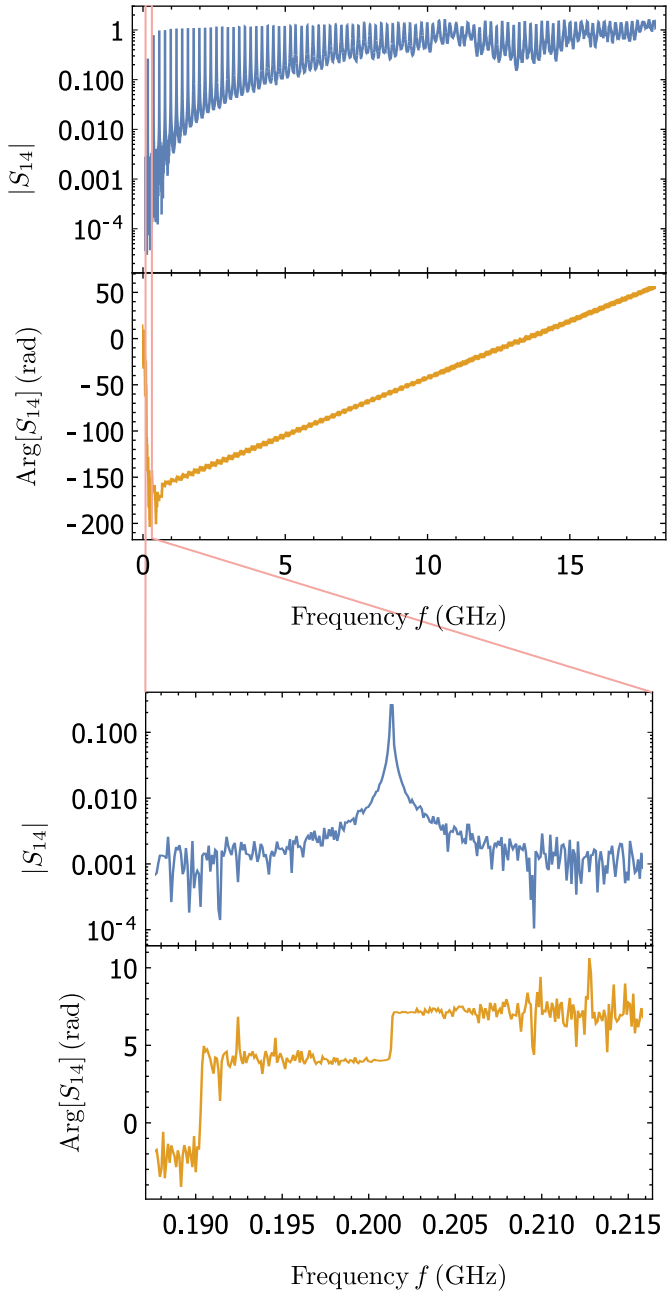

Figure 4.5: Transmission coefficient spectrum for CPW resonator LFCPW06.

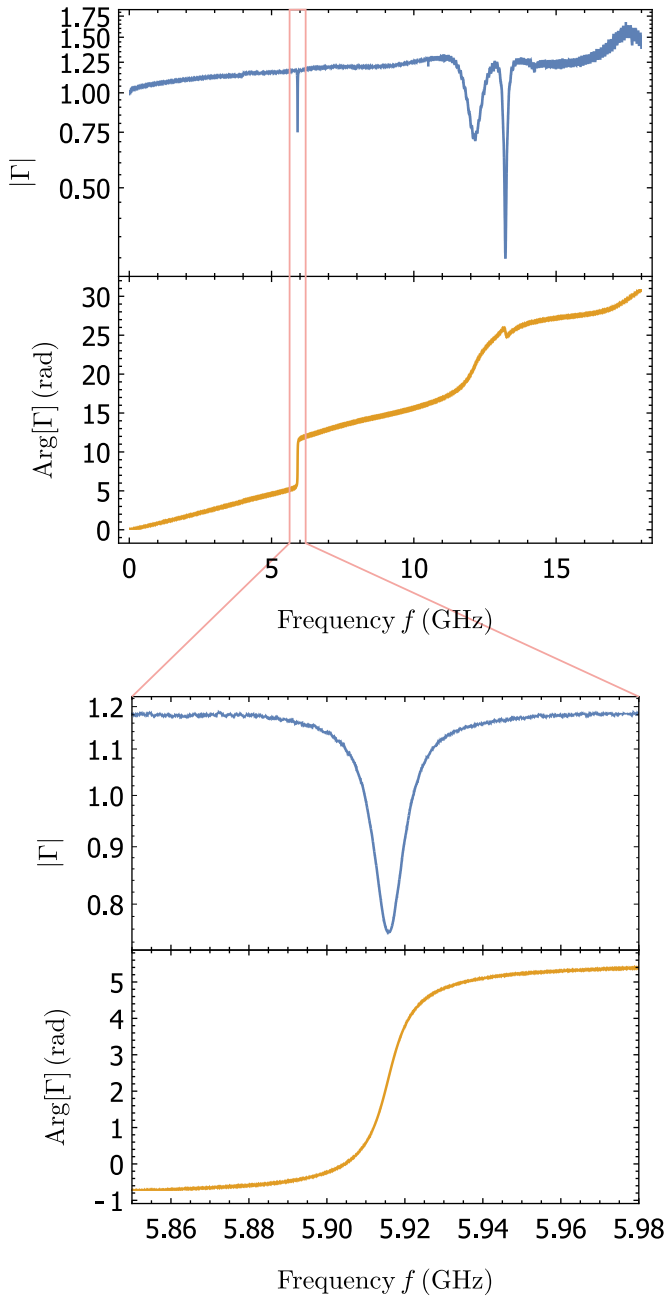

Figure 4.6: Measurement of reflection coeffiecient Γ spectrum for lumped-element resonator LFLEM04_04. See table 3.2 for design parameters. Note the zoom-in plot is a separate measurement trace to achieve a higher point density.

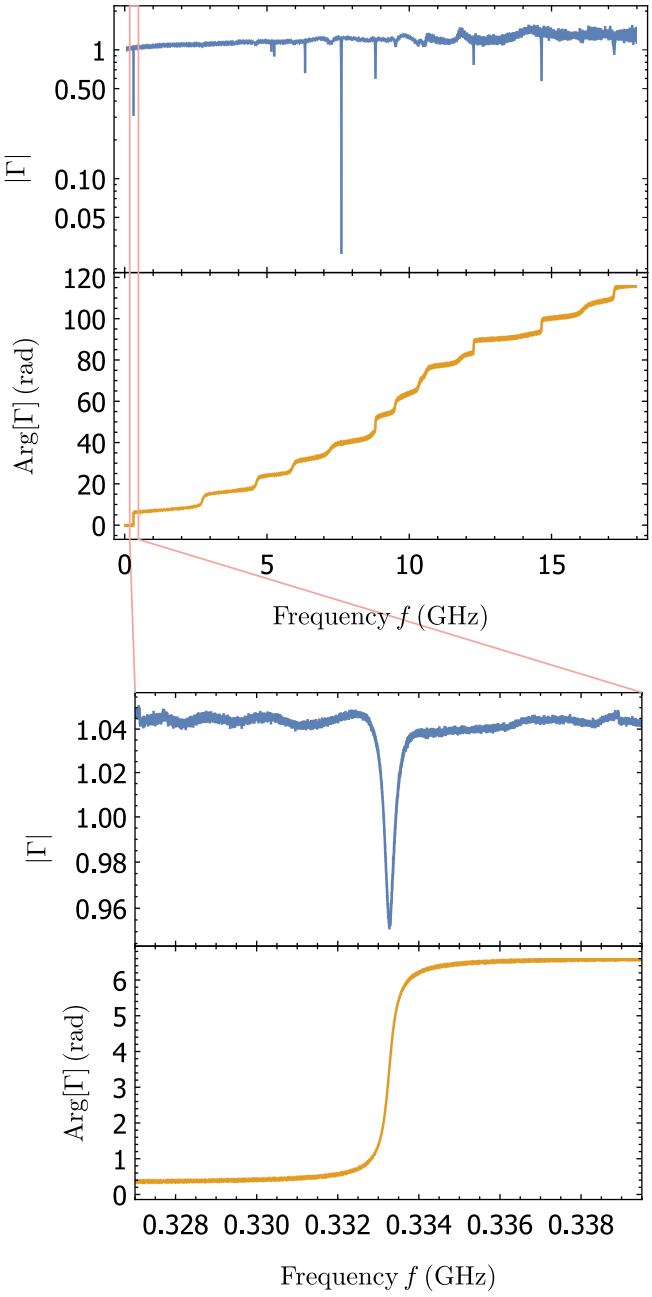

Figure 4.7: Reflection coefficient Γ spectrum for lumped-element resonator LFLEM04_16.

shows the accuracy to which our model in section 2.3.5 estimated the fundamental resonance frequencies. More detailed analysis is left for chapter 5. Note that S_{11} for these devices extends beyond 0 dB substantially. For these raw measurements, the background was not removed. It is sensible the reflection coefficient would be above 1 because the attenuation constant of the cables at 4.2 K is less than at room temperature. Further, note that the accompanying plots of the fundamental resonance have a much smaller point density so that the resonances can be clearly resolved when fitting, and that the background is removed when fitting these fundamental resonances in section 5.1.2.

Chapter 5

Data Analysis and Results

After gathering raw data for the scattering matrix elements $S_{ij}(f)$ of the different resonators as a function of frequency using the VNA, the data is imported into *Mathematica* and analyzed in order to extract the values of the physical properties characterizing the resonators. Those properties are given by the resonance peaks in the data (see figures 4.6, 4.7, 4.4 and 4.5). Measurements have been done of the full spectra with high enough point density (see section 4.3.2) allowing the data close to the resonances to be fitted according to physical models of resonances (see equation (5.1) for the transmission measurements of the CPW devices and (5.8) for the reflection measurements of the LE devices). This process and the results obtained from it are discussed in detail in this chapter.

5.1 Fitting Procedures

As the CPW resonators have been measured in transmission compared to reflection for the LE resonators, the fitting procedures are different, even though the underlying physical models (for the near-resonance behavior) are both based on a lumped element description. The fitting procedures give the following results (for each resonance/mode):

- Resonance frequency f_0
- Loaded quality factor Q_L
- Coupling rate κ (just for LE)
- Loss rate γ (just for LE).

An overview of all the results and comparison to design parameters is shown in table 5.2 for the LE and table 5.1 for the CPW resonators.

5.1.1 Coplanar Waveguide Resonators

The transmission coefficient for CPW resonators can be fully described by the transmission matrix method [12], but near resonance, it can be described with a lumped-element model. It was with this model that the data was fit. A

capacitively-coupled CPW resonator has a transmission spectrum S_{21} near resonance described by

$$S_{21} = e^{i\phi}\left(\frac{A}{1+4Q_L^2\left(\frac{f}{f_0}-1\right)^2} + x_0 - i\left(\frac{2AQ_L\left(\frac{f}{f_0}-1\right)}{1+4Q_L^2\left(\frac{f}{f_0}-1\right)^2} + y_0\right)\right), \quad (5.1)$$

where f_0 is the resonance frequency, Q_L is the loaded quality factor, and $A = \kappa/(\kappa+\gamma) \in \mathbb{R}$ is the ratio of coupling rate to total (coupling and environmental) loss rate. The parameters x_0 and y_0 are a complex offset to S_{21} at DC, similar to the offset described in section 5.1.2. The QuDev *Mathematica* library "WaveguideCavityCoaxFunctions.nb" implements functions to fit data to this model using the *Mathematica* function `NonlinearModelFit` .

To obtain an accurate fit, it is important to include data at least 3 dB on both sides of the resonance. Because the cavity is measured in transmission, amplitude information is usually sufficient to estimate Q_L and f_0. A good calibration (see section 4.2) is necessary to accurately estimate T_0 and thus distinguish Q_{int} and Q_{ext}. As the dipstick measurement procedure does not provide a sufficient calibration, only Q_L and f_0 are extracted from the transmission spectra. Methods used to estimate Q_{int} and Q_{ext} for CPW resonators are described in section 5.2.2.

A key difference between fitting in transmission and reflection is two-fold: first, phase noise away from resonance is greater in transmission because the amplitudes are nearer the noise floor of the network, resulting in less reliable phase fits [11]. Second, the suppressed amplitude information away from resonance in transmission makes fitting $|S|$ more reliable than in reflection. This is because in reflection, the background amplitude is above the noise floor away from resonance. Though amplitude is most informative in transmission, estimates from fitting a complex Lorentzian as in equation 5.1 yields comparable values of physical parameters as fitting only amplitude, but additionally give phase and circle comparisons to data, as seen in figure 5.1. Note that amplitude information is effected more significantly by the changing temperature of the environment in transmission. So contrary to reflection measurements, carrying out background measurements in transmission (as done for reflection measurements described in section 4.2) is not useful.

5.1.2 Lumped Element

From the measured frequency range the range to be processed by the fitting algorithm is manually selected in order to give a reasonable fit result. This is not a trivial task because the physical model for the reflection coefficient is only valid close to the resonance, however, given that they match the model, more points result in better fits.

The fitting procedure is the one used in [13] which is based on [11]. In this subsection the procedure is explained and demonstrated on an example measurement of the resonator LFLEM04_16 which is designed to have a frequency of 300 MHz at an impedance of $Z = 170\,\Omega$ (see table 3.2).

For doing the actual fitting in the steps described below to the corresponding data the *Mathematica* function `NonlinearModelFit` is used which returns the

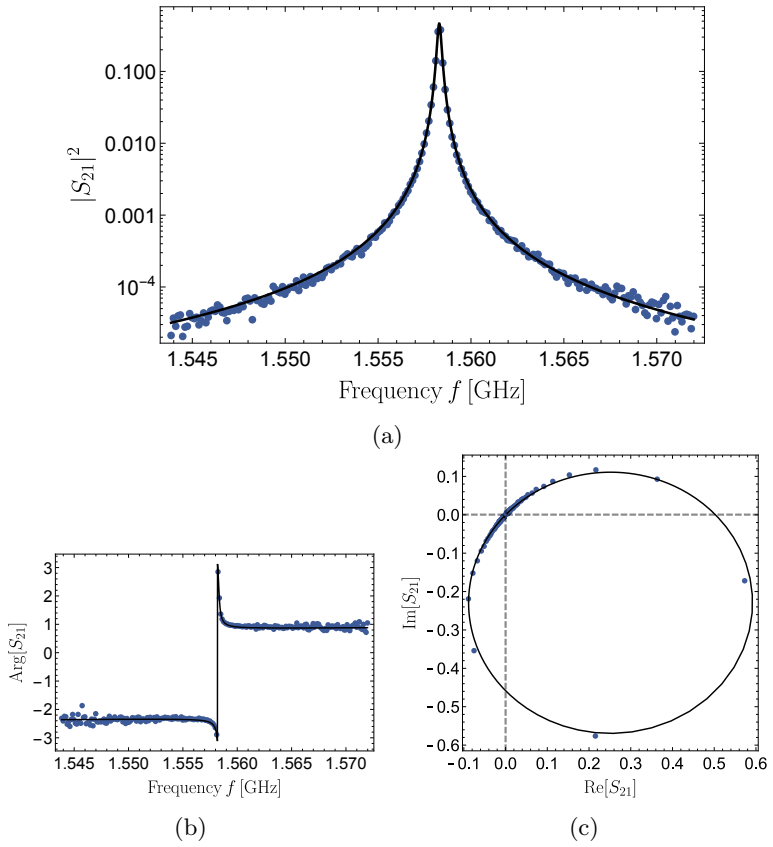

Figure 5.1: Complex Lorentzian fit (black line) of S_{21} data (points) using equation 5.1 for coplanar waveguide LFCPW02. (a) $|S_{21}|^2$ on log-scale, (b) Arg[S_{21}] and (c) Polar Plot of S_{21}.

fit parameters as well as error estimates. For the first resonance of each device, which has been measured with high point density, the background is subtracted as described section 4.2, otherwise $S_{ii}(f)$ as used in the following sections is assumed to be the raw data.

Circle Fit

The plot of imaginary versus real part of the reflection coefficient results in a circle with center on the real axis. In the ideal case the circle would intersect the real axis at zero and at the resonance (corresponding to the largest absolute value). The circle can alternatively be represented with the origin as center (this is done in the first two steps of this fitting procedure). In reality two corrections have to be introduced: first a rotation, that is a phase shift, due to a difference in the reference planes of measurement and coupling and second a translation due to crosstalk [11]. Those two corrections are determined using this first step in the fitting procedure. The data

$$\{\mathrm{Re}(S_{ii}(f)), \mathrm{Im}(S_{ii}(f))\} \tag{5.2}$$

is therefore fitted using the model

$$f_{\mathrm{circ}}[x_0, y_0, R](x, y) = (x - x_0)^2 + (y - y_0)^2 - R^2. \tag{5.3}$$

Starting values are determined by simple geometric estimations. Figure 5.2 shows the data and circle fit.

As mentioned above the physical models used apply only near resonances, hence data close to the resonance is weighted more. In order to achieve that, the *reference point*, which lies opposite to the one corresponding to the resonance, is determined: It can be approximately found by finding the point between the first and last datapoint, as it can be assumed that S_{ii} changes slowly with frequency far away from a resonance. The weights are then chosen as the fourth power of the distance from the reference point [11].

The fit parameters x_0, y_0 and R including error estimates as well as the reference point are found in this step.

Phase Fit

Using the results from the first step the data is corrected (see discussion above and figure 5.3): The circle is shifted such that the center lies at the origin and then rotated such that the reference point lies on the positive real axis. This gives the corrected reflection coefficient

$$\tilde{S}_{ii}(f) = e^{-i\phi_{\mathrm{rot}}}(S_{ii}(f) - (x_0 + iy_0)). \tag{5.4}$$

Additionally, any 2π-jumps in phase are removed in order to obtain smooth phase data.

The argument of the corrected reflection coefficient $\mathrm{Arg}(\tilde{S}_{ii}(f))$ is fitted according to the model

$$\phi[\phi_0, \tau, f_0, Q_L](f) = -\phi_0 - \tau f - 2\arctan\left(2Q_L\left(1 - \frac{f}{f_0}\right)\right) \tag{5.5}$$

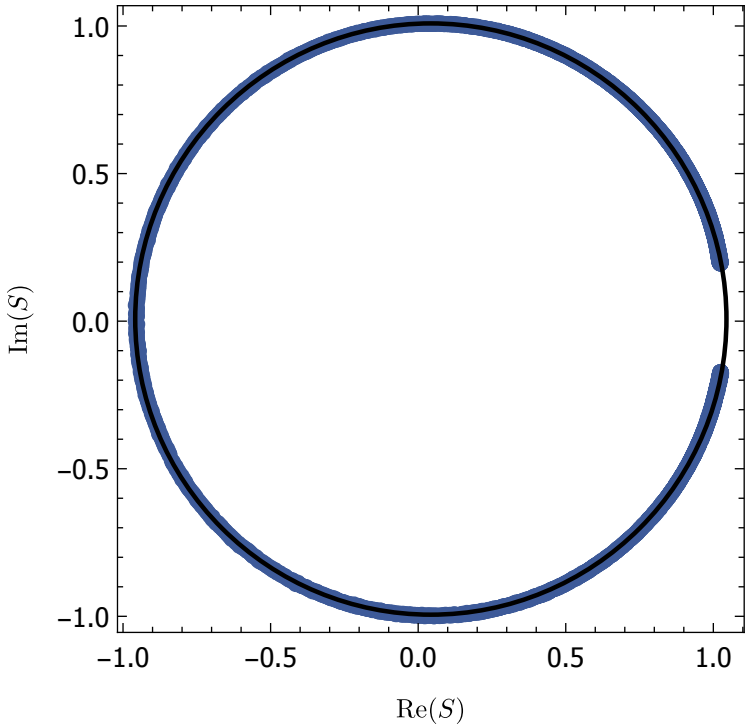

Figure 5.2: Imaginary versus real part and circle fit (equation (5.3)) of the complex reflection coefficient $S_{ii}(f)$. The origin and radius are determined from the fit.

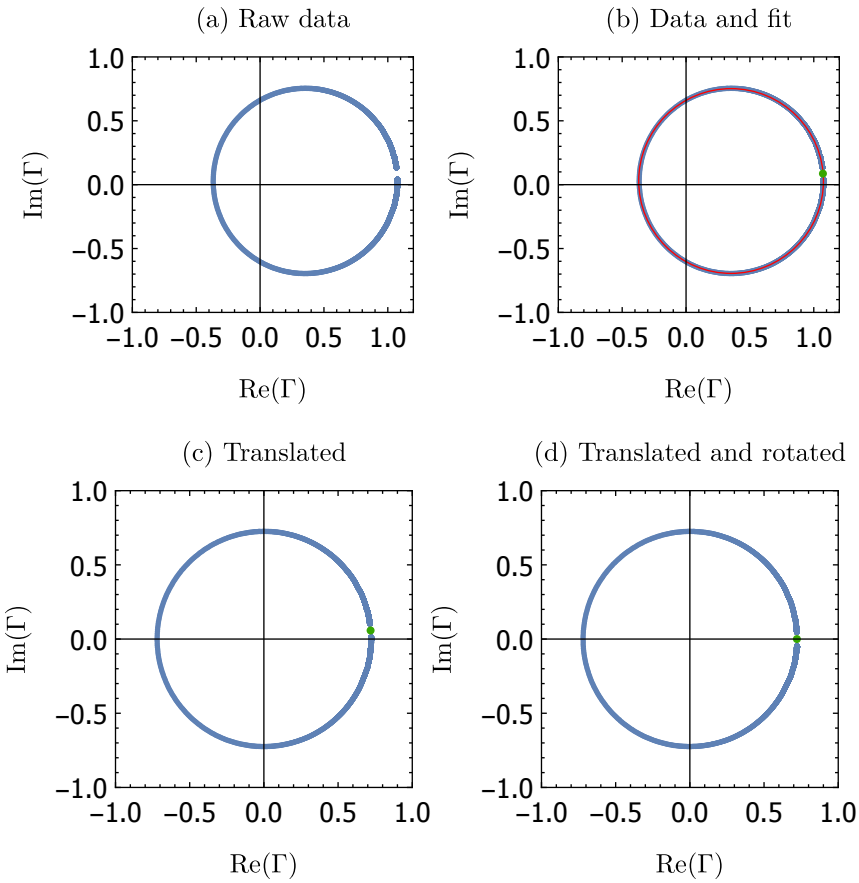

Figure 5.3: Process of data correction shown at an example measurement (LFLEM07_11). A plot showing imaginary versus real part of the reflection coefficient for (a) raw data in blue, (b) data and circle fit (red) (see section 5.1.2). The reference point is shown in green. First the data is translated to the center (c) and then rotated (d) such that the reference point lies on the positive real axis.

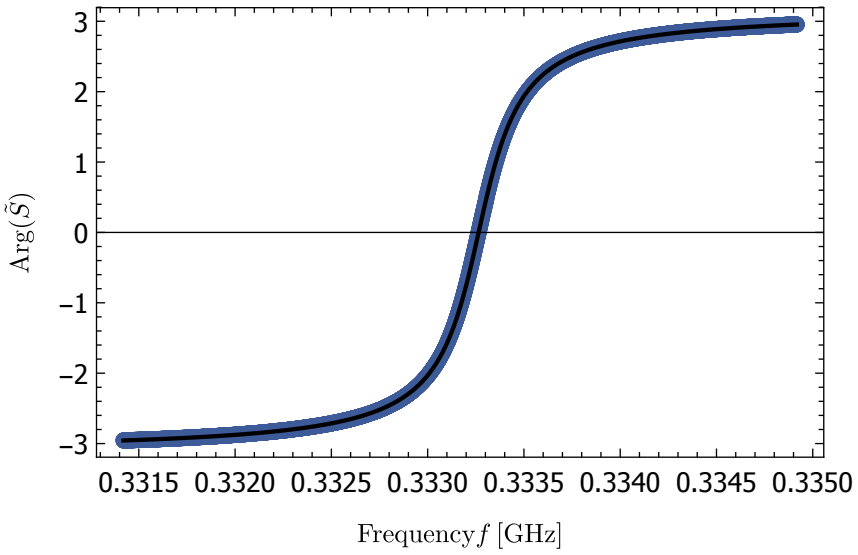

Figure 5.4: Phase data and fit according to equation (5.5) of the corrected complex reflection coefficient.

and using $\phi_0 = \tau = 0$, $f_0 = \text{argmin}_f \{S_{ii}(f)\}$ and $Q_L = f_0/\text{FWHM}$ as starting values. See figure 5.4 for a plot of data and fit function. From the fit parameters estimates for the external and internal quality factor can be extracted:

$$Q_{\text{ext}} = \frac{Q_L}{|R|}, \tag{5.6}$$

$$Q_{\text{int}} = \frac{1}{\frac{1}{Q_L} - \frac{1}{Q_{\text{ext}}}}, \tag{5.7}$$

where R is the radius from the circle fit. However, due to the calibration problem discussed in section 4.2, the obtained values for coupling and loss rate might not be accurate [13].

Complex Lorentzian Fit

In order to obtain more accurate values for the coupling and loss rate, the effect of the non-cryogenic calibration is taken into account by considering a normalization as well as an offset term. Based on input-output theory the following expression for the reflection coefficient can be found [13]

$$S_{11}^{\text{IO}}[A, \kappa, f_0, Q_L](f) = -A\left(\frac{\kappa}{\frac{f_0}{2Q_L} - i(f - f_0)} - 1\right). \tag{5.8}$$

This expression is fitted to the rotated complex reflection data, resulting in the amplitude A, the coupling rate κ, the resonance frequency f_0, the loaded quality factor Q_L and the loss rate

$$\frac{\gamma}{2\pi} = \frac{f_0}{Q_L} - \frac{\kappa}{2\pi}. \tag{5.9}$$

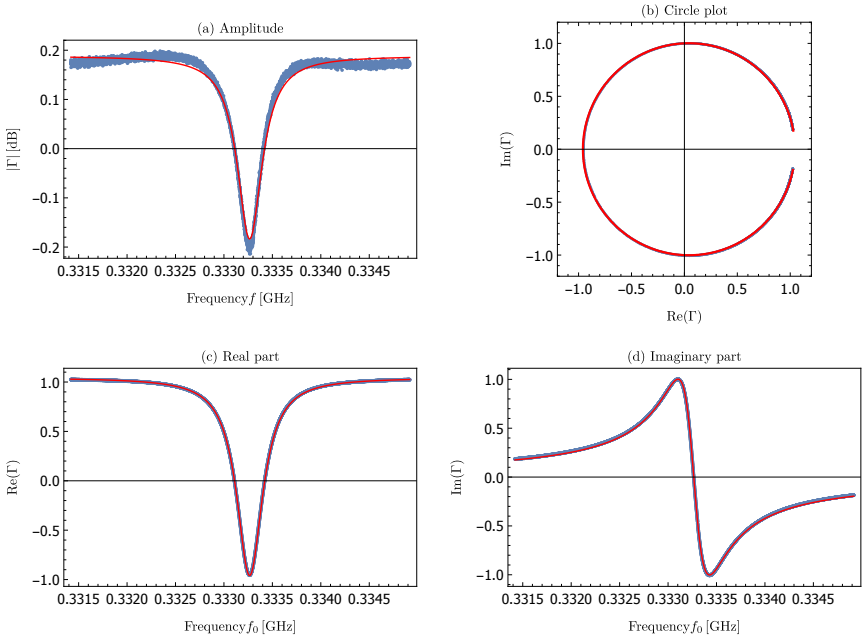

Figure 5.5: Complex Lorentzian fit based on equation (5.8) done on the corrected data. This fit can be used to extract coupling and loss rates. The plots show example data (blue points) and fit functions (red lines) for (a) the absolute part, (b) polar representation, (c) real and (d) imaginary part of the complex reflection coefficient.

5.2 Further Analysis and Post Processing

After analyzing all the measured resonator spectra by fitting the separate resonances, the properties which characterize the resonators are compared for the different resonators. That is the dependence on the parameters which have been varied in the designs is investigated. The fundamental mode characterizes the basic properties of the resonator, that is frequency, coupling and losses. However, the behavior for higher frequencies is also important; therefore, the higher order resonances and their spacing is also analyzed. All those results are presented in this section. A more detailed discussion follows in the next chapter in section 6.1.

5.2.1 Lumped Element

The first step is a comparison of designed and the corresponding measured quantities: frequency f_0 (figure 5.6) and coupling rate κ (figure 5.8). Data from all the measured resonators except for number 15 is shown (see table 3.2 and section 4.3.1). One can conclude that the frequency of the fundamental resonance can be predicted accurately enough for design purposes, the linear fit function shown in the figure is given by

$$f_0^{\text{meas}} = 1.010(8) \cdot f_0^{\text{des}} \tag{5.10}$$

		First Mode		Second Mode	
Name	f_0^{d} **[GHz]**	f_0^{m} **[GHz]**	Q_L^{m}	f_1^{m} **[GHz]**	$Q_{L,1}^{\mathrm{m}}$
LFCPW02	1.56	1.55829	6510	3.11568	3390
LFCPW03	0.951	0.948113	6550	1.89626	3670
LFCPW04	0.626	0.622419	6180	1.2459	4090
LFCPW05	0.333	0.170292	4000	0.510925	3230
LFCPW06	0.202	0.20133	4180	0.402756	3920

Table 5.1: Fit Results for the coplanar waveguide resonators, analogous to table 5.2. The fit parameters f_0^m and Q_L^m for the first two modes are given. Note the discrepancy in f_0^d and f_0^m for LFCPW05. This device was found to have a fabrication defect which split the fundamental mode in two by half: $f_1^m - f_0^m = 340\,[MHz] \approx f_0^d$.

	Design Values		First Mode				Second Mode	
Nr.	f_0^{d} **[GHz]**	$Q_{\mathrm{ext}}^{\mathrm{d}}$	f_0^{m} **[GHz]**	Q_L^{m}	κ^{m} **[MHz]**	γ^{m} **[MHz]**	f_1^{m} **[GHz]**	$Q_{L,1}^{\mathrm{m}}$
01	5.96	100000	5.97828	2430	0.0602(2)	2.399(8)		
02	5.96	10000	5.9492	2210	0.2301(5)	2.4646(9)		
03	5.96	1000	5.94297	1530	1.4485(2)	2.4420(4)		
04	5.96	100	5.91581	490	9.9146(6)	2.1801(9)	12.1712	10
05	3.02	100000	3.20404	4010	0.0224(2)	0.776(1)		
06	3.02	10000	3.20261	3510	0.11575(2)	0.7956(2)		
07	3.02	1000	3.18766	2100	0.74184(1)	0.7737(2)	16.9591	280
08	3.02	100	3.15713	570	4.8780(5)	0.6969(5)	16.1426	390
09	0.998	100000	1.10395	9360	0.00563(7)	0.1124(1)		
10	0.998	10000	1.10185	7610	0.03144(1)	0.11343(9)		
11	0.998	1000	1.09715	3280	0.22426(5)	0.1098(2)	7.56996	130
12	0.998	100	1.09025	790	1.27318(5)	0.10609(7)	7.32793	40
13	0.302	100000	0.337752	22240	0.001158(9)	0.0140(1)	2.8955	2370
14	0.302	10000	0.33689	13560	0.00849(2)	0.01635(1)	4.68878	840
15	0.302	1000	0.33565	190	0.0763(4)	1.736(5)	2.80457	100
16	0.302	100	0.333265	1020	0.31263(3)	0.01338(3)	2.74931	20
23	2.85	1000	2.6564	3020	0.38996(4)	0.4884(2)		
24	2.99	1000	3.10253	2320	0.62647(4)	0.7086(2)		

Table 5.2: Fit results for the lumped element resonators given by their number (see table 3.2). The values for the frequency f_0^{m}, coupling κ^{m} and loss rate γ^{m}, where the superscript m denotes experimental values, obtained from fitting the resonances in the reflection spectrum are compared to the design values for frequency f_0^{d} and external quality factor $Q_{\mathrm{ext}}^{\mathrm{d}}$ (the superscript d standing for "designed"). The coupling and loss rate of the first mode of resonator 15 are to be considered unphysical, as there was some kind of measurement problem for that mode (see discussion in section 5.2.1).

and has a coefficient of determination

$$R^2 = 0.999066. \tag{5.11}$$

Figure 5.7 shows the relative difference between measured and designed frequency as a function of designed frequency. One can see that the error is on the order of magnitude of 10% for the low frequency resonators and decreases for higher frequencies. This is still acceptable for design accuracy, as the accuracy of the design equations is in that range. The fact that the relative error increases with decreasing frequency might pose a problem for even lower frequencies, but can probably avoided when using a more accurate prediction model.

The measured coupling rate does show a linear dependence on the designed one, however it is smaller by about a factor of approximately 5 to 6, which can be seen from the slope of the linear fit function given by

$$\frac{\kappa^{\text{meas}}}{2\pi} = 0.180(3) \cdot \frac{\kappa^{\text{des}}}{2\pi} + 0.02(5)\,\text{MHz} \tag{5.12}$$

with coefficient of determination $R^2 = 0.996528$.

The dependence of loss rate and loaded quality factor on the resonance frequency of the resonator is shown in figures 5.9 and 5.10. The loss rate increases with increasing frequency and is not significantly dependent on the external quality factor, which is made clear by the fact that there are just clusters for each frequency even though data from all the measured resonators except for number 15 is shown (see table 3.2 and section 4.3.1). Two phenomenological fit models are proposed and compared: a power fit

$$\frac{\gamma^{\text{meas}}}{2\pi} = \left(0.27(3)\,\text{GHz}^{-1} \cdot f_0^{\text{des}}\right)^{1.86(8)}\,\text{MHz} + 0.00(3)\,\text{MHz} \tag{5.13}$$

and an exponential fit

$$\frac{\gamma^{\text{meas}}}{2\pi} = 0.5(1)\,\text{MHz} \cdot \text{e}^{0.29(3)\,\text{GHz}^{-1} \cdot f_0^{\text{des}}} - 0.6(1)\,\text{MHz}; \tag{5.14}$$

and are seen to be in very good agreement with the data. The logarithmic plot (figure 5.9b) suggests that the power law fits better to the data, however statistical measures (see table 5.3 for a comparison of those for the two different models) such as the Bayesian information criterion show that even though it is slightly better this is not conclusive enough to rule out the exponential model.

As can be expected from the above described behavior and the relationships

$$\frac{1}{Q_L} = \frac{1}{Q_{\text{ext}}} + \frac{1}{Q_{\text{int}}} \tag{5.15}$$

and

$$\frac{\gamma}{2\pi} = \frac{f_0}{Q_{\text{int}}}, \tag{5.16}$$

the loaded quality factor decreases with increasing frequency and with decreasing external quality factor.

The relations given by equations (5.15) and (5.16) are verified by plotting and fitting the inverse of the directly measured loaded quality factor versus

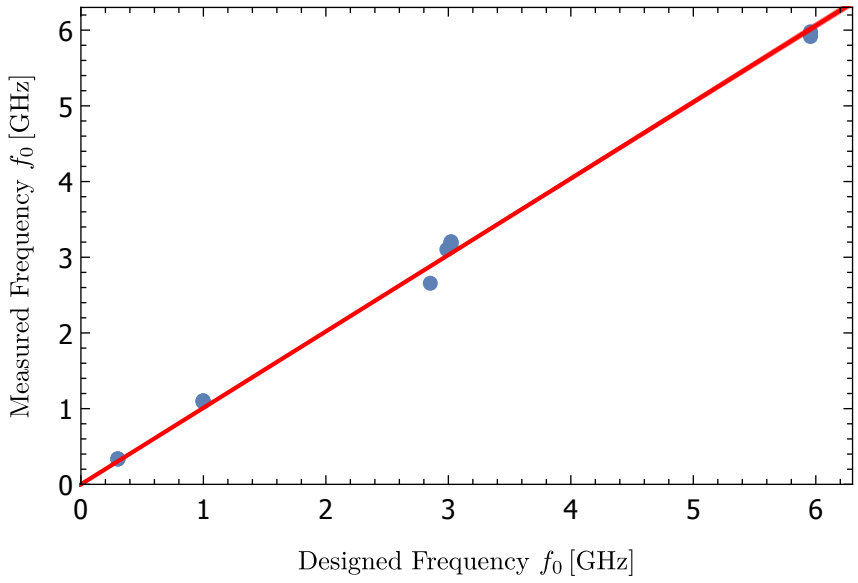

Figure 5.6: Comparison of measured and designed frequency f_0 of the LE resonators. The red line is a linear fit, the confidence band is shown in light red. This shows that the frequency of the first resonance can be predicted accurately enough for design purposes.

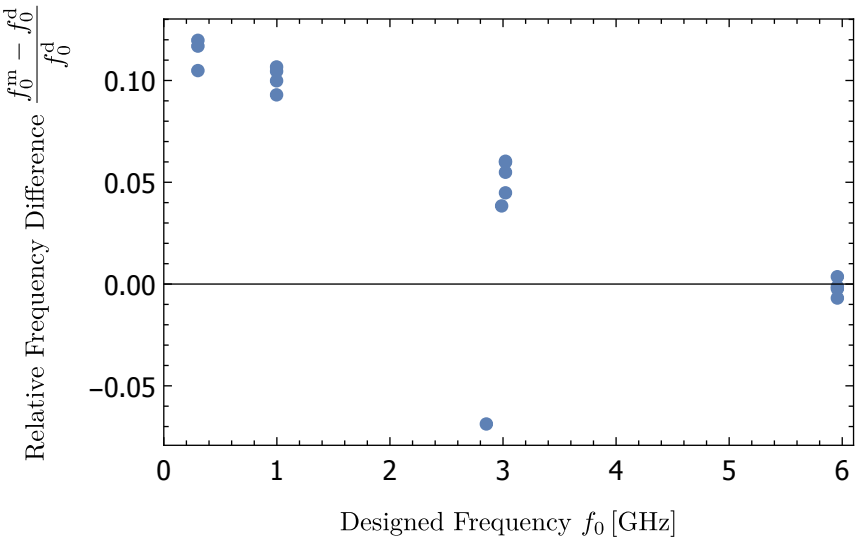

Figure 5.7: Relative difference between measured and designed frequency as a function of designed frequency. One can see that the relative errors increase with decreasing frequency. However, the errors are at most in the order of 10%, which is what can be expected from the accuracy of the design equations.

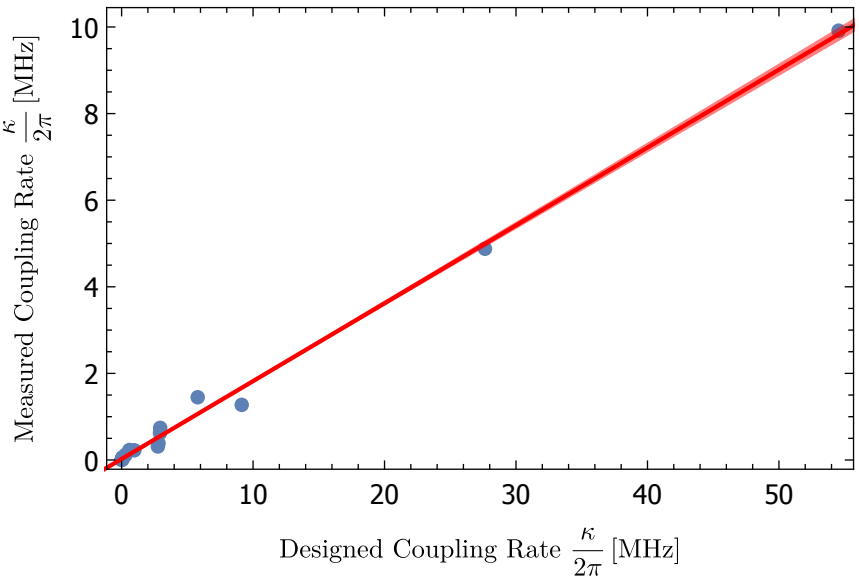

Figure 5.8: Comparison of measured and designed coupling rate κ of the LE resonators. The red line is a linear fit, the confidence band is shown in light red. The axes scaling makes clear that there is a significant (systematic) mismatch between designed and measured coupling rate.

	Statistical Measures		
Fit Model	R^2	**BIC**	**AIC**
$(af_0)^b + c$	0.9981	−40.01	−43.35
$ae^{bf_0} + c$	0.9979	−38.13	−41.46

Table 5.3: Statistical measures for the two fit models of the loss rate as a function of measured frequency. The coefficient of determination R^2 shows how well both models agree with the data and the Akaike (AIC) and Bayesian (BIC) Information Criterion suggest that the power law is slightly better (their values being smaller for that model); however, due to the small difference, no conclusive evidence against the exponential law can be identified.

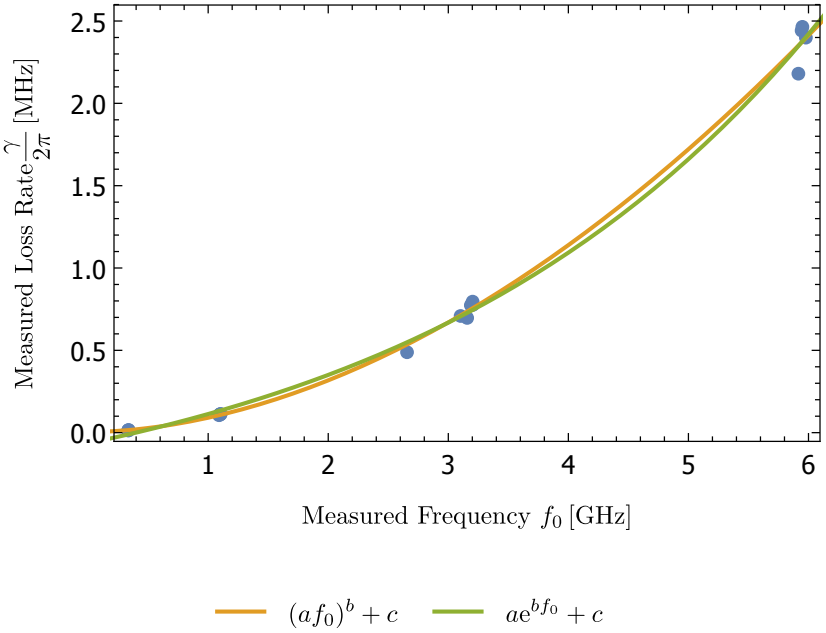

(a) Linear scale.

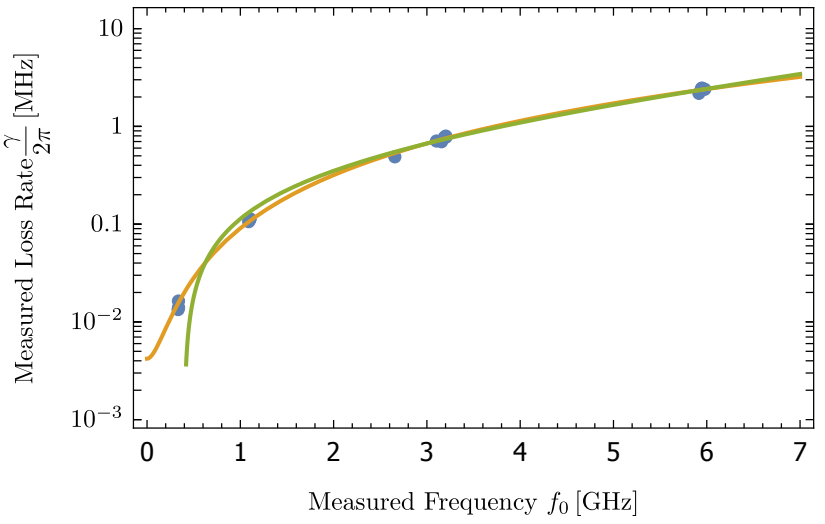

(b) Logarithmic scale.

Figure 5.9: Measured loss rate γ (from the Lorentzian fit given by equation (5.8)) of LE resonators with different frequency f_0 and designed external quality factor Q_{ext}. As expected, the loss rate can be seen to be largely independent of the external quality factor and increases with increasing frequency. Two different fit models have been proposed and are shown in the plot: an power law (yellow) and an exponential law (green).

	Fit Parameters		
f_0 [GHz]	a	b	$\frac{\gamma}{2\pi}$ [MHz]
0.3	0.092(2)	$0.5(1) \cdot 10^{-4}$	0.016(3)
1	0.113(5)	$1.4(3) \cdot 10^{-4}$	0.14(3)
3	0.151(6)	$2.6(3) \cdot 10^{-4}$	0.78(8)
6	0.160(5)	$4.5(3) \cdot 10^{-4}$	2.7(2)

Table 5.4: Resulting fit parameters and error estimates for the fit model $\frac{1}{Q_L} = \frac{a}{Q_{\text{ext}}} + b$. The fact that a is not equal to 1 is consistent with the mismatch of measured and designed coupling rate κ (see figure 5.8). The parameter b can be interpreted as the inverse of the internal quality factor, hence $\frac{\gamma}{2\pi} = f_0 \cdot b$.

the inverse of the designed external quality factor for resonators of different frequencies as shown in figure 5.11a. The fit model has the form

$$\frac{1}{Q_L} = \frac{a}{Q_{\text{ext}}} + b \tag{5.17}$$

and the fit parameters found for the resonators of different frequency f_0 are shown in table 5.4. Equation (5.16) allows the calculation of the loss rate from the fit parameters; the values obtained like that agree with the values extracted via single-resonance fitting as demonstrated by figure 5.11b. The systematic mismatch between designed and measured coupling rate as shown in figure 5.8 is not a problem for this method, because the relationship between measured and designed inverse external quality factor turns is linear according to that plot and the mismatch is taken account of by the additional fit parameter a, which would not be necessary otherwise (ideally it holds that $a = 1$). This method of determining the loss rate is therefore not completely independent from the Complex Lorentzian fit, but the overlap is very small (basically just the conclusion $\kappa^{\text{m}} \propto \kappa^{\text{d}}$). It still allows a consistency check for γ and even for the mismatch in coupling rate as shown in table 5.4.

Figures 5.12 concerns the higher order modes. Those are modes that are actually not expected from the simple lumped element model, but are still present as spurious modes. The terms *higher order modes*, *higher order resonances* and *spurious modes* are used interchangeably in the context of lumped element devices in this text. The modes are numbered according to frequency in ascending order starting with $n = 1$ for the fundamental resonance; this leads to a different interpretation of the *mode number* n than in the case of coplanar waveguide resonators, where the mode number has actual physical meaning. The term *mode number* is used throughout this text. Comparing the behavior of those for the 1 GHz and the 300 MHz resonators one can see that for high coupling, that is external quality factors of 100 and 1000, the effect of the external quality factor on the first few higher order modes is very small. Only when going higher in mode number or external quality factor can significant deviations be seen; however, no clear trend is identifiable. The spectrum of the device with $Q_{\text{ext}} = 10^5$ shows a step-like behavior, where two modes are very close together and every second matches the corresponding mode of the $Q_{\text{ext}} = 10^4$ device.

Concerning the quality factor of higher order modes, at first no clear trend can be observed. However, the ratio of the standard deviation and mean of the

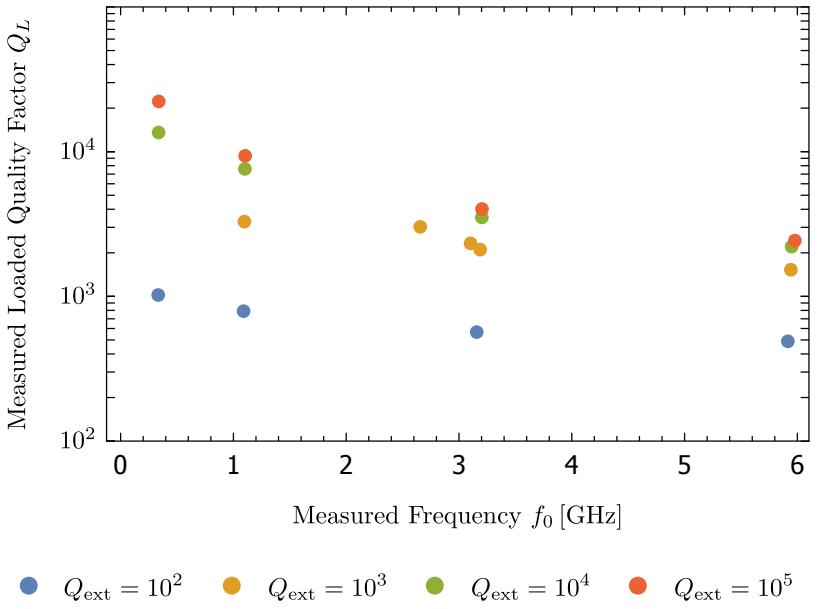

Figure 5.10: Measured loaded quality factor Q_L as a function of the frequency f_0 for LE resonators with different designed external quality factors Q_{ext}.

set of loaded quality factors across mode number for a given resonator

$$\frac{\sqrt{\text{Var}\left(\{Q_{L,n}\}_{n>1}\right)}}{\langle\{Q_{L,n}\}_{n>1}\rangle}, \tag{5.18}$$

as shown in figure 5.13, shows a clearly decreasing trend with increasing external quality factor for the 300 MHz resonator. This could imply interesting behavior of Q_{int} as a function of mode number and might be helpful in identifying the spurious modes.

At this point resonator 15 (LFLEM03_15) is discussed. As previously mentioned its data has been excluded from all plots concerning coupling or loss rate (or derived quantities). The reason for that is that there was some kind of measurement problem in the measurement of the first mode (see figure 5.14), which resulted in the complex Lorentzian fit giving unreasonable values for anything but the frequency. A problem like that was not encountered in any of the other measurements not even for the higher order resonances of the same device. The other fit results of this devices should still be treated with care, however the produced error in the frequency seems to be comparably small.

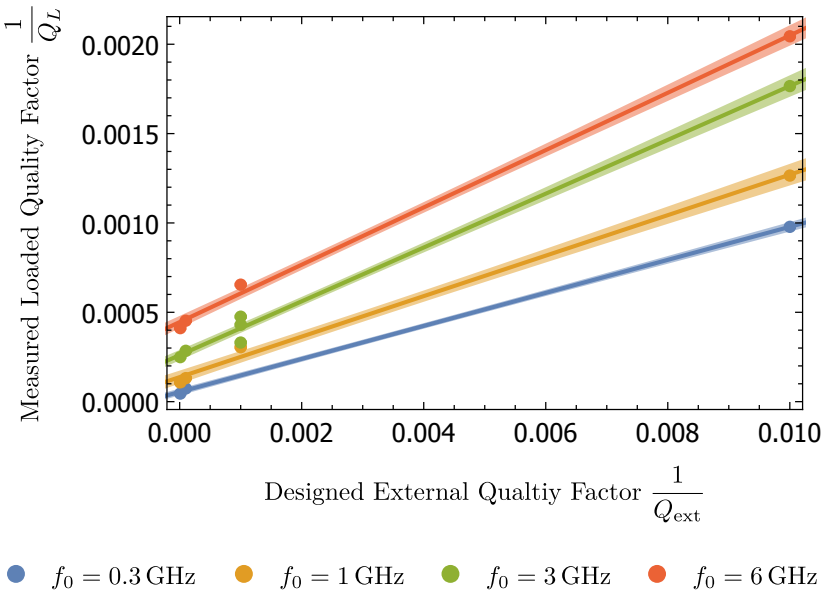

(a) Measured Q_L as a function of designed Q_{ext}. Linear fits according to equation (5.15) are shown in the respective colors including confidence bands.

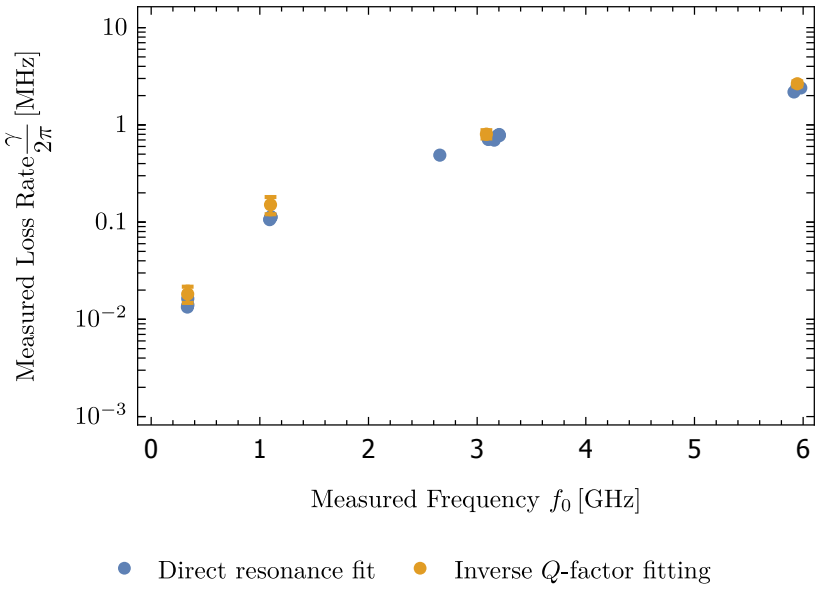

(b) Extracting the offset in the fits (see table 5.4) shown in (a) the loss rate can be found (yellow). Those results seem to agree quite well with the values found directly by fitting single resonances (blue).

Figure 5.11: Loaded quality factor and loss rate for LE resonators with different frequency f_0.

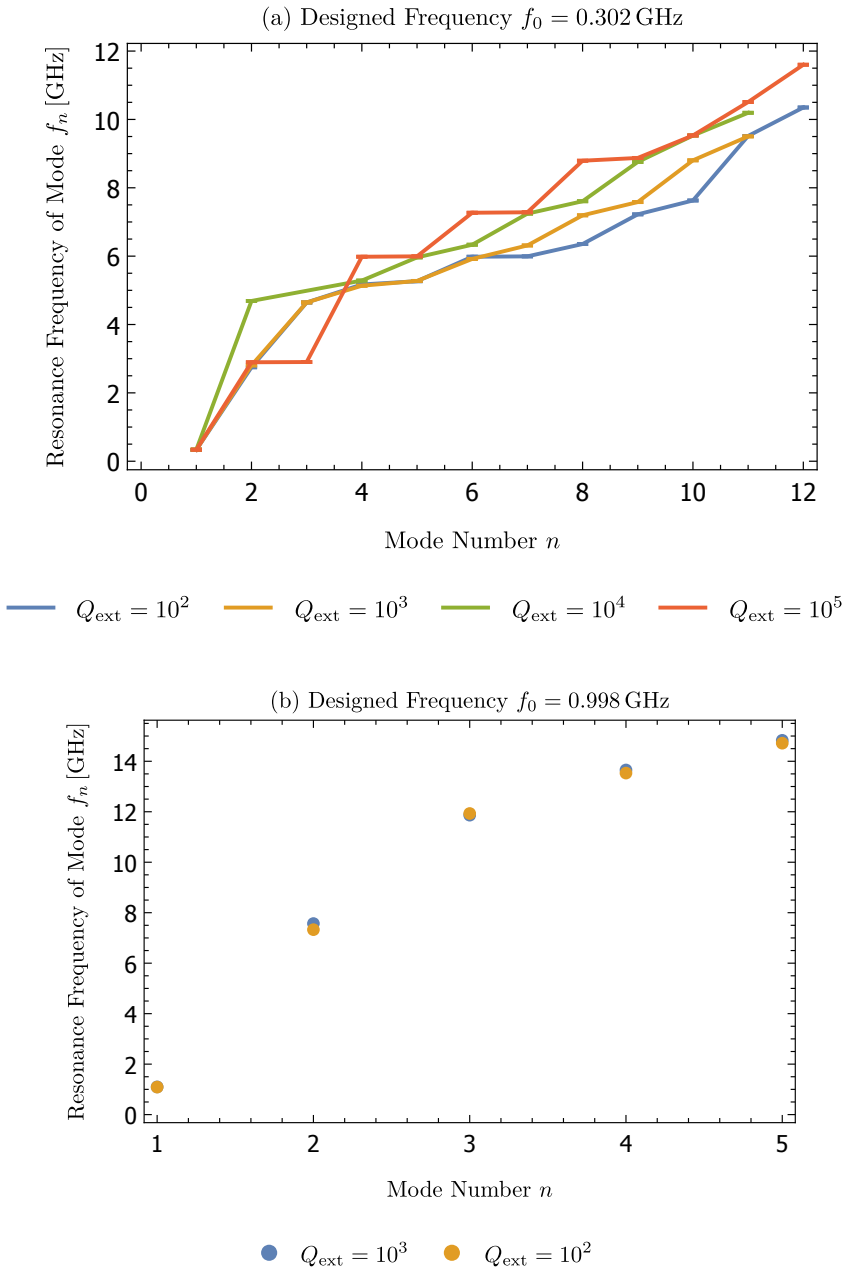

Figure 5.12: Frequency versus mode number for LE resonators with different designed fundamental frequency and external quality factor. The behavior is quite different for the 0.3 GHz resonator compared to the 1 GHz, not only as a function of mode number but also considering how relevant the external Q factor is. See table 3.2 for the resonator names and numbers corresponding to the data points shown in these plots.

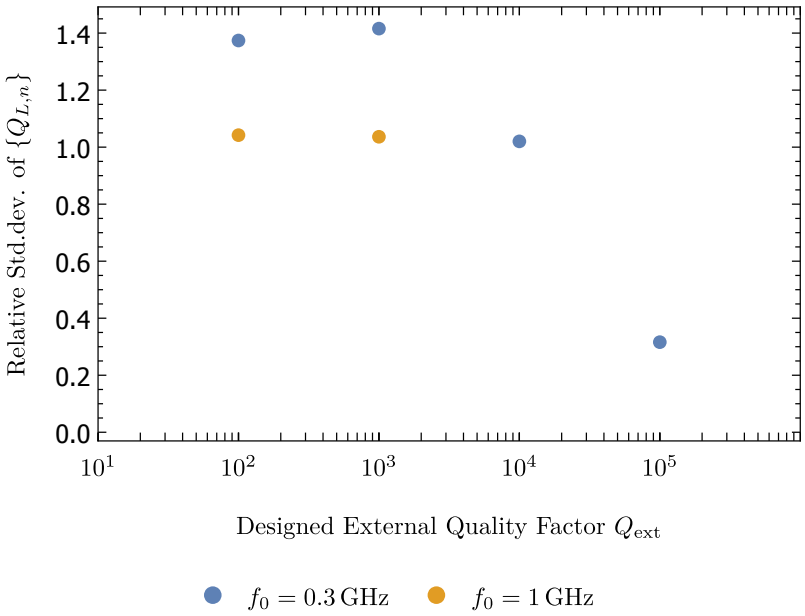

Figure 5.13: Relative standard deviation of the loaded quality factors $\sqrt{\text{Var}(\{Q_{L,n}\})}/\langle\{Q_{L,n}\}\rangle$ for LE resonators with different designed fundamental frequency and external quality factors. (excluding the fundamental resonance).

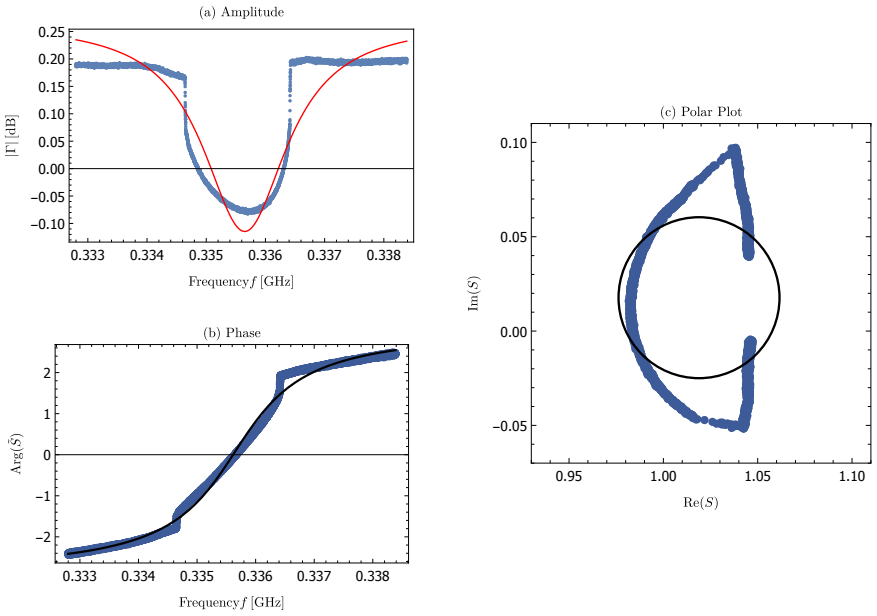

Figure 5.14: Fits of the fundamental resonance of resonator 15 showing the measurement problem.

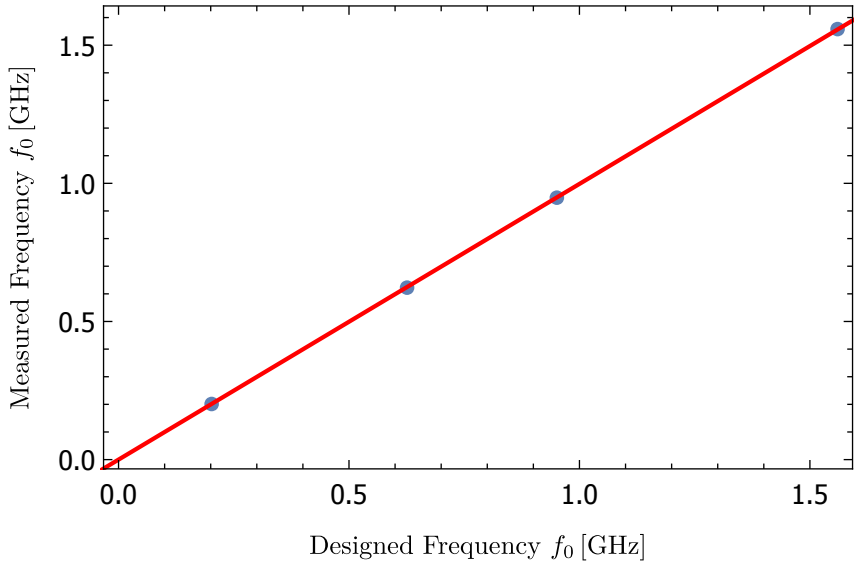

Figure 5.15: Comparison of measured and designed fundamental frequency f_0 of the CPW resonators. The red line is a linear fit as given in equation (5.19), the confidence band is shown in light red. Similar to figure 5.6, CPW resonators are accurately designed to low fundamental resonances.

5.2.2 Coplanar Waveguide

As in the previous section, the data analysis to characterize the CPW resonators is three-fold. First we consider the design efficacy of the fundamental resonance frequency f_0. The measured frequency f_0^{meas} is plotted against the designed frequency f_0^{des} in figure 5.15. The linear fit $f_0^{\text{meas}} = a \cdot f_0^{\text{des}}$ plotted in the figure is

$$f_0^{\text{meas}} = 0.9979(9) \cdot f_0^{\text{des}}, \tag{5.19}$$

and has a coefficient of determination

$$R^2 = 0.999998, \tag{5.20}$$

demonstrating a high accuracy in the design of CPW resonators even to low frequencies at QuDev. As this geometry has been used extensively in cQED, this is expected. Note however that LFCPW05 is excluded from figure 5.15 due to an error in fabrication which split the fundamental mode in two (see table 5.1).

The second physical parameter to understand in these devices is the loaded quality factor Q_{L} and its dependence on f_0. The physical model for Q_{L} is obtained using the following relations given in equations (2.19). Note that in the experiments, the feed line and resonator line impedances were equal ($R_L = Z_0 = 50\,\Omega$).

Because Q_{ext} was designed to be constant for all devices at the fundamental

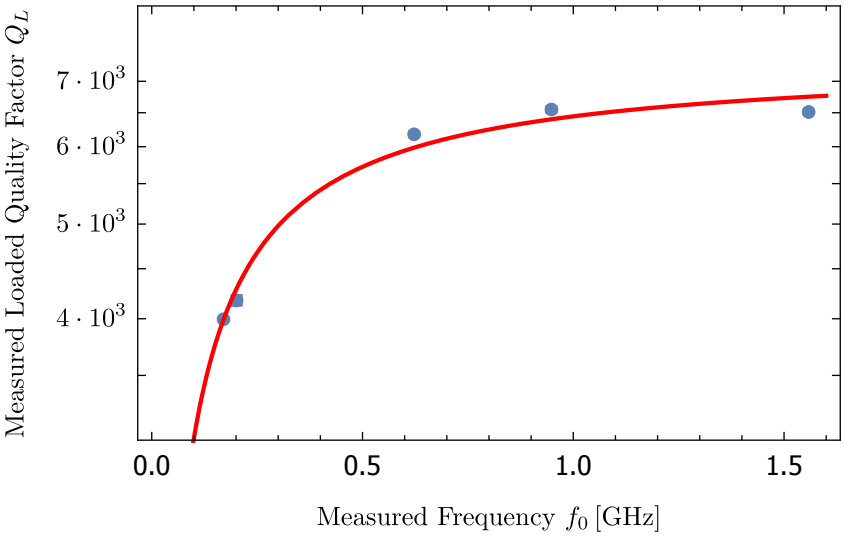

Figure 5.16: The loaded quality factor Q_L for the fundamental resonance f_0 for the measured CPW devices. The fit (line) corresponds to the function determined in equation (5.22).

mode ($n = 1$), one can compare Q_L for each device's f_0 to a simplified model:

$$Q_\mathrm{L}^{-1} = Q_\mathrm{int}^{-1} + Q_\mathrm{ext}^{-1} = \frac{\gamma}{\omega_0} + A,$$
$$Q_\mathrm{L} = \frac{f_0}{\gamma/2\pi + A f_0}. \tag{5.21}$$

It should be stressed that α is presumed to vary insignificantly in this narrow frequency range for this analysis. This is justified by comparison with the next analysis (see 5.6) which relaxes this assumption. The resulting function when fitting the data to equation (5.21) is

$$Q_L\,(f_0)^\mathrm{meas} = \frac{f_0^\mathrm{meas}}{20(2)\,\mathrm{kHz} + 1.36(4) \cdot 10^{-4} f_0^\mathrm{meas}}, \tag{5.22}$$

where the fit parameters are in linear rather than angular units, and is plotted in figures 5.16. The difference between the model and the data in figure 5.16 shows that assuming constant Q_ext between devices is not a perfect description (fit residuals were on the order of 5%). This disagreement is reasonably within the precision of designing Q_ext for a CPW resonator.

The third step in further analysis of the CPW resonators is to consider the higher-order modes (HOMs). As these resonators are distributed-element, effectively 1-D resonators, their HOMs are rather simple: $f_n = n \cdot f_0$. The resonance f_n of several HOMs measured for each device is plotted against mode number n in figure 5.17. Linear fits to these data sets are given in table 5.5. In contrast to the previous analysis, extracting γ for each device does not assume α to be frequency independent. The measurements agree quite well, with the exception of

	Fit $f_n = m \cdot n$	
Name	f_0 **[GHz]**	m **[GHz]**
LFCPW02	1.56	1.5579(2)
LFCPW03	0.951	0.94784(9)
LFCPW04	0.626	0.6211(2)
LFCPW06	0.202	0.20068(6)

Table 5.5: Fit values of the HOM behavior of the CPW resonators. The data are consistent with the 1-D distributed-element resonator model of these devices.

	Fit Parameters	
Name	C_κ **[fF]**	$\gamma/2\pi$ **[kHz]**
LFCPW03	33.8(5)	20(5)
LFCPW04	47.9(3)	30(2)
LFCPW06	135.5(7)	29(1)

Table 5.6: Fit values of $Q_\mathrm{L}(f_n)$ corresponding to equation (5.23b) for two of the CPW resonators.

the fundamental frequency for LFCPW05 (see table 5.1). Interestingly, despite the fabrication error, scaling with mode number is consistent with the designed f_0^d. However, the measured f_0^m is about half of f_0^d. This can also be observed in table 5.5 which gives the values of the linear fit $f_n = m \cdot n$.

Using the HOM data for a resonator, and the physical model given in equations (2.19), it is possible to estimate Q_int by fitting $Q_\mathrm{L}(f_n)$ despite poor calibration if one assumes to know C. We rewrite equations 2.19 as

$$\begin{aligned} Q_\mathrm{int} &= \frac{f_n}{(\gamma/2\pi)}, \\ Q_\mathrm{ext} &= \frac{\pi R_\mathrm{L} \cdot C \left(1 + (\pi R_\mathrm{L} C_\kappa)^2 f_n^2\right)}{(\pi R_\mathrm{L} C_\kappa)^2 f_n} \end{aligned} \tag{5.23a}$$

$$\Rightarrow\ Q_\mathrm{L} = \frac{\pi R_\mathrm{L} \cdot C \left(1 + (\pi R_\mathrm{L} C_\kappa)^2 f_n^2\right)}{(\pi R_\mathrm{L} C_\kappa)^2} \left(\frac{1}{f_n + (\gamma/2\pi)\, \frac{\pi R_\mathrm{L} \cdot C \left(1+(\pi R_\mathrm{L} C_\kappa)^2 f_n^2\right)}{(\pi R_\mathrm{L} C_\kappa)^2 f_n}} \right), \tag{5.23b}$$

where C_κ and γ are fit and $C = C_\ell \ell/2$ is estimated for each device using equation (2.12). This was done for three devices for which sufficient HOM data had been obtained, with the fits and data shown in figure 5.18. Parameter values corresponding to the fit plots can be found in table 5.6. It is notable that the fit C_κ from this data agree with estimates of C_κ to within 13%, and γ, which is assumed constant, agrees within 50% between devices and with the result from the fit used earlier to produce figure 5.16.

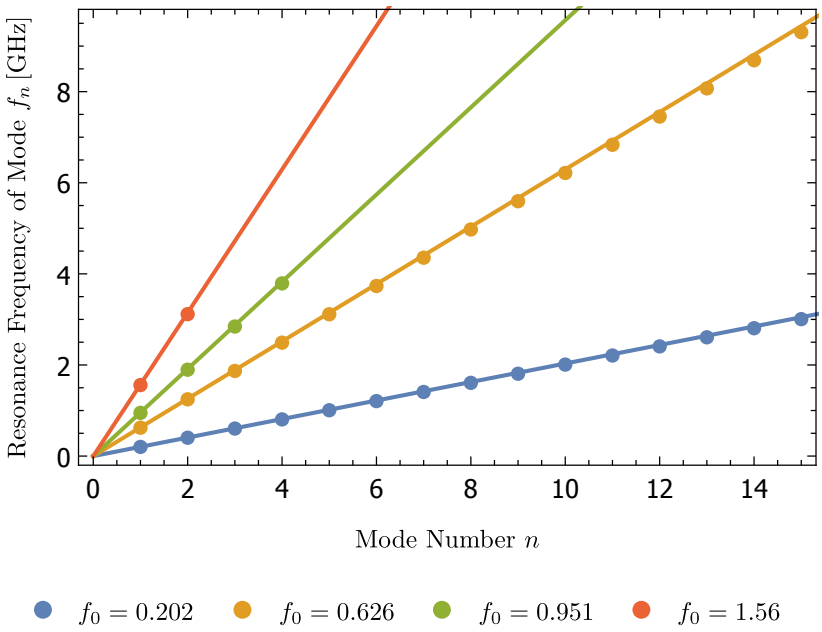

Figure 5.17: Higher order mode frequencies versus mode number n for all CPW devices. The colored lines show theoretical models; parameters from linear fits (not plotted) are given in table 5.5.

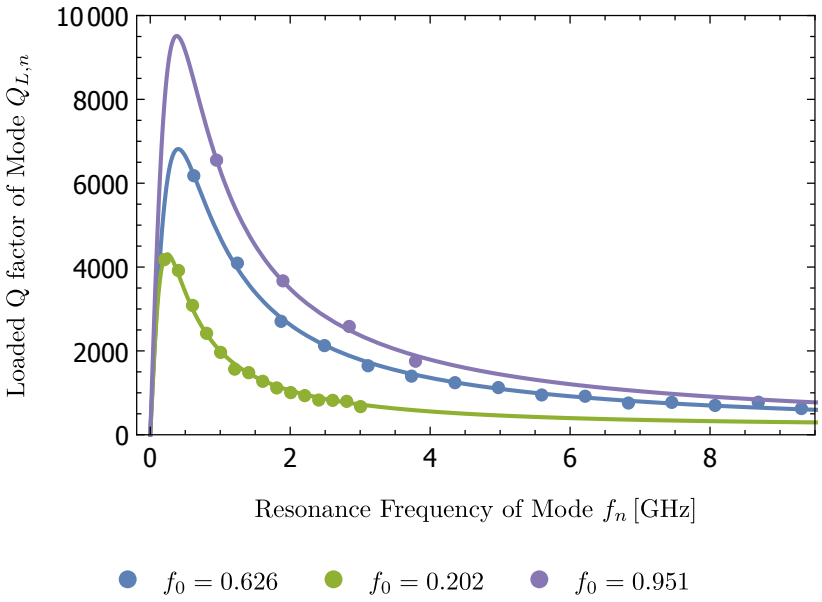

Figure 5.18: Loaded quality factor as a function of resonance frequency f_n for mode n. Green is LFCPW06, purple is LFCPW03, and blue is LFCPW04. The fits correspond to the fit function (5.23b).

Chapter 6

Discussion and Outlook

6.1 Discussion

In this section the results presented in chapter 5 (tables 5.2 and 5.1 and section 5.2) are discussed in more detail. The properties of resonators with *compact resonator design* are compared to those of the established CPW resonator design.

6.1.1 Design Accuracy

Generally, the design accuracy for the fundamental frequency is satisfactory for guiding future designs. For the coplanar waveguide designs this had been expected, as they are well understood and established. However, the established design routines of the lab have usually been used for resonators of a very different order of magnitude in frequency. Referring to figure 5.15 and the fit given by equation (5.19) with coefficient of determination in equation (5.20) one can conclude that the routines work well, even for very large CPW resonators such as LFCPW06.

For the lumped element resonators it is of greater importance that the simple model used in the description, a basic LC resonator (see section 5.15), even though any capacitance to ground has been neglected, and the estimation formulae for inductance and capacitance as described in section 2.3 give such accurate predictions in the investigated frequency range. The typical deviations were on the order of 10% (see figure 5.7), which is also the highest accuracy that can be expected from the estimation formulae used. This results in a good match as shown in figure 5.6 and demonstrated by the coefficient of determination (equation (5.11)) for the linear fit (5.10).

The design of the coupling rate for the LE resonators do not agree with the measured rates being consistently smaller than the designed ones by a factor of approximately 5. As discussed in section 2.3.5, the actual circuit model includes additional capacitances to ground. Either the model with C_g and $C_{g,p}$ numerically used or the simpler model with just the series capacitance to ground can explain a possible decrease in effective coupling. In the simple analytical model the actual measured coupling rate $\tilde{\kappa}$ can be seen to be reduced to approximately $\kappa/5$, where $\kappa \propto C_\kappa^2$ (see equation (2.45)) is the coupling rate expected from just

C_κ, if C_g is of the order of magnitude of C_κ, which is consistent with the assumptions made above (see equation (2.43)). This and the fact that the design accuracy of the frequency is quite high justifies that $C_g \ll C$. A geometrical model to predict C_g and $C_{g,p}$ is a next step to design the pack-arranged lumped element resonator more accurately.

6.1.2 Quality Factor and Loss

The loaded quality factor Q_L as a function of the fundamental frequency shows very different behaviors for lumped element and coplanar waveguide resonators. While it decreases with increasing frequency in the case of the former, it increases for the latter as predicted by equation (5.21). For direct comparison see figure 6.1, which overlays the measured CPW data in table 5.6 onto figure 5.11.

For the lumped element resonators the loss rate has been consistently extracted in two different ways and a phenomenologically motivated power law has successfully been fitted to the obtained values. The main observation is that in contrast to the coplanar waveguide geometry, where no clear trend in the loss rate as a function of frequency is observed (which is most likely due to the small frequency range investigated the overcoupling to the devices), the loss rate decreases with decreasing frequency, giving insight into the question about loss rate as a function of frequency that was posed in chapter 1. It is interesting to note that the exponent is rather close to 2, which is what is expected in the case of quasiparticle-dominated loss. Experiments to study the loss rate γ at lower temperatures would shed more light on its origins for these devices.

6.1.3 Higher Order Resonances (Full Spectra)

The spectrum of higher order (or spurious) modes is an interesting and important aspect of any resonator, especially from a practical point of view. Comparing the spectra of low frequency lumped element and coplanar waveguide resonators in figures 4.7 and 4.5, it is quite clear that, for cases where only the fundamental mode is relevant and the higher order ones introduce problems, the lumped element resonator seems to provide the better spectrum. Shown in figure 6.2 is the scaling of the spurious modes for the lumped element devices relative to their fundamental resonances. This visualization highlights the mode structure as frequency and coupling is varied. It suggests that the scaling of the next spurious mode becomes smaller as the fundamental resonance is increased for these devices. Additionally, some modes appear missing for the same resonators with different couplings. In these cases, the data did not suggest strongly enough that a mode was present, either because it could not be fit or very weak coupling to such modes, making them difficult to identify. Referring to table 5.2 and figure 6.2, one can see that usually the first higher order mode is around 5 to 8 times the fundamental frequency for resonators with f_0 in the range of 300 MHz to 3 GHz. This is certainly a much larger spacing than in the spectra of CPW resonators, where the modes are equally spaced in steps of the fundamental frequency, which leads to spacings of the order of a few hundred Megahertz for low frequency resonators. This dense mode spacing is not ideal for single-mode optomechanical coupling. However, the fact that the spectrum of lumped element resonators is not yet understood leads to problems as those higher order modes cannot yet be predicted. The understanding of the

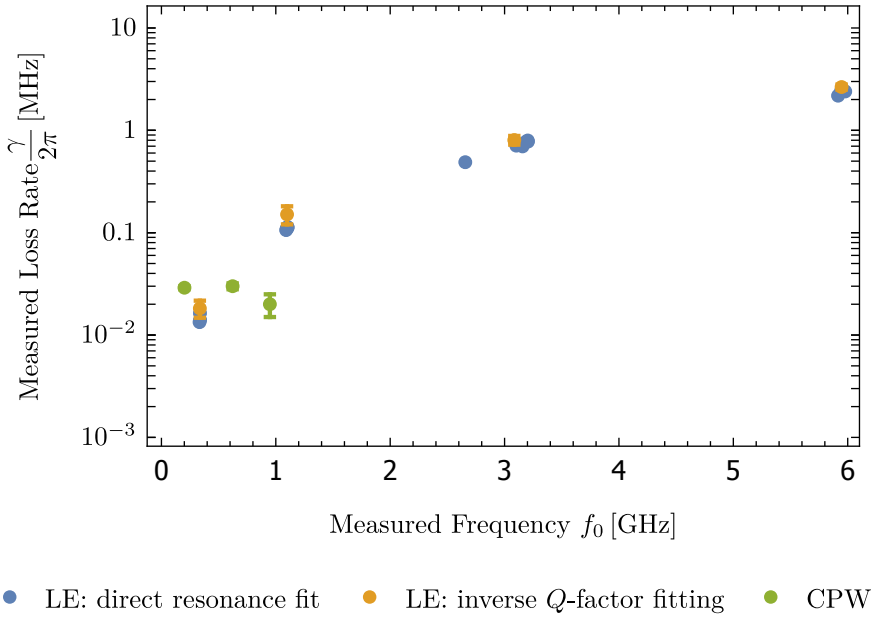

Figure 6.1: Loss rate γ versus f_0, both LE and CPW
Overlay of figure 5.11 with the CPW loss rate data obtained from the fits shown in figure 5.18

CPW spectrum, on the other hand, is well-established. The equal spacing of the higher order modes in CPW resonators has been verified and is shown in figure 5.17. The higher order resonances in the lumped element resonators are most likely spurious modes caused by parts of the circuit resonating at their respective self resonance frequency, which needs more investigation for actually identifying them. An alternative way to look at them would be by identifying the paired modes as a single split mode. The spectra have also been checked for common modes that could possibly have originated from other parts of the setup, such as the PCB or PCB shield. However, no pair of modes f_i, f_j was found to match the following criteria:

- the resonators are on the same PCB,
- $\Delta f = |f_i - f_j| < \langle \mathrm{FWHM} \rangle_{i,j}$
- $\Delta\mathrm{FWHM} = |\mathrm{FWHM}_i - \mathrm{FWHM}_j| < \frac{1}{10} \langle \mathrm{FWHM} \rangle_{i,j}$

An interesting feature that has been observed in lumped element resonators is the behavior of the loaded quality factor as a function of mode number and external quality factor: Looking at the relative standard deviation, that is the ratio of the standard deviation to the average, while excluding the fundamental mode, a clear trend of decreasing fluctuation can be identified (see figure 5.13). For the coplanar waveguide resonators on the other hand the established relationship [7] of decreasing quality factor with resonance mode number was verified to acceptable agreement (see figure 5.18).

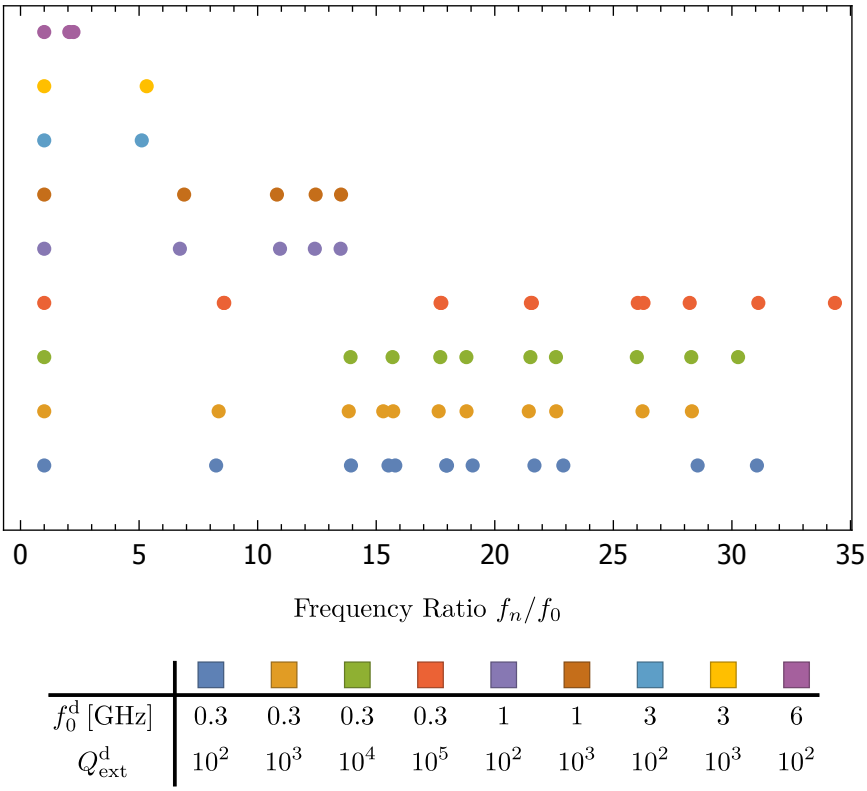

Figure 6.2: The spurious mode spacing for the lumped element devices relative to their fundamental resonance. The points are stacked according to frequency and coupling.

6.2 Outlook

In order to decide whether the lumped element design type considered in this work (see section 3.2.4) can be useful, some open questions have yet to be answered. The effects of non-grounding have to be investigated further, in particular its effect on both the coupling rate and the frequency has to be understood in more detail. Otherwise the open questions concern their properties at frequencies greater than their fundamental resonance; the spurious resonances and their origins are not well understood in this thesis and require additional experimental and theoretical investigation. However, there are also some questions concerning the effect of the non-grounding on the frequency and to what degree the neglected coupling between superturns introduces inaccuracies or additional features. The results presented indicate a power law for the loss rate as a function of fundamental frequency. This has to be verified further and possible theoretical explanations have to be discussed. The observed behavior of the variance of the loaded quality factor as a function of coupling too is still to be explained.

6.2.1 Coupling and Optomechanics Analogy

The lumped element design has been done with the possibility in mind of coupling the resonator inductively to a microwave resonator in the fashion shown in figure 1.2. The part of the supermeander inductor (see section 3.2.1) pointing towards the outside of the compact resonator (see section 3.2.4) is implemented in a flexible way and allows adding structures for inductive coupling at those places.

Though there are theoretical proposals to optomechanically couple two coplanar waveguide resonators [8], the lumped element designs offer more space efficiency and possibly higher magnetic field localization for inductive coupling. Furthermore, the LE resonators are better-suited for low-frequency mechanical oscillator analogues over CPW devices due to their higher spacing between the fundamental resonance and spurious modes.

Because we are interested in high zero-point-fluctuations of the flux $\hat{\phi} = M\hat{I}$ through the squid loop from the low-frequency resonator to achieve strong optomechanical coupling, it is of interest to maximize the current fluctuations $I^r_{\mathrm{ZPF}} = \Phi^{\mathrm{r}}_{\mathrm{ZPF}}/L_r$ in the LF resonator. The largest that the mutual inductance M can be is $M = \sqrt{L_\mu L_r}$, so the maximum flux fluctuations in the HF resonator (denoted by the index μ for microwave) from the LF resonator (denoted by the index r for radio) is given by

$$\begin{aligned}\Phi^{\mu}_{\mathrm{ZPF}} &= M I^{\mathrm{r}}_{\mathrm{ZPF}} \\ &= \sqrt{L_\mu L_r}\frac{\Phi^{\mathrm{r}}_{\mathrm{ZPF}}}{L_r} \\ &= \sqrt{\frac{L_\mu 2\hbar Z_{\mathrm{r}}}{L_r}} \\ &= \sqrt{2\hbar L_\mu \omega_{\mathrm{r}}}.\end{aligned}$$

Future setups with LF resonators which will be actively cooled optomechanically must take this coupling into account for design considerations.

6.2.2 Next Steps

As a first step further design investigations are necessary: The open questions mentioned above have to be answered. Further experiments and theoretical considerations are necessary to either prevent, compensate or account for the effects of non grounding on frequency and coupling rate.

There are several different possibilities on how to proceed: The resonator can just be grounded in parallel to C_g, however, in that case the effect of $C_{g,p}$ on the frequency is not negligible anymore as can be seen from analysis of the impedance of that circuit. In that case $C_{g,p}$ would have to be decreased in order to justify neglecting it. Alternatively, it can be tried to minimize $C_{g,p}$ while estimating C_g from geometrical parameters. Further studies where the geometrical parameters are varied instead of the physical ones could be helpful in understanding further effects of non-grounding, coupling between superturns and other special geometrical features of the proposed design.

In order to understand the spurious modes, simulations or laser spectroscopy could be useful in addition to standard network analysis experiments. Additionally, the fabricated devices that have not been measured can be used to do further experiments that can help understand the design.

Before deciding for lumped element or coplanar waveguide, one could also try out the Hilbert curve design, which is already manufactured, too. The following studies are ready to be done using the fabricated but not measured devices

- LE: systematic impedance and coupling study ($Z \in \{50, 100, 170, 300\}\,\Omega$ and $Q_{\text{ext}} \in \{10^3, 10^4, 10^5\}$)
- CPW: variation of turning radius ($r \in \{50, 100, 150\}\,\mu$m)
- CPW: Hilbert curve design

A next step would implement a Hamiltonian analogous to the one of *Optomechanics*, that is a parametric coupling of a low to a high frequency resonator. This could be done by terminating the high frequency resonator with a Josephson junction which can then be coupled inductively to the inductor of the low frequency resonator (see figure 1.2). The proposed design is optimized for this type of coupling, because it provides good access to the inductor. In a last step, resonator cooling could be done, as explained in section 1.2.1.

Acknowledgments

First of all we would like to thank the principal investigator at QuDev Prof. Dr. Andreas Wallraff, for the opportunity to do such an interesting, instructional and rather unusual semester project. Additional thanks go to him for the very deep and interesting discussions at different stages of the project and for the useful advice given during those.

Many thanks go to our supervisor, Dr. Anton Potočnik, who was able to provide excellent advice and help throughout the project. We would also like to thank him for producing our mask and our devices, for wire-bonding them to the PCBs and for manually putting air bridges on one of our devices. We also thank him for proofreading this thesis and providing many helpful comments and suggestions to enhance the text.

Further thanks regarding device fabrication and work in the clean room go to Michele Collodo and Mintu Mondal. We thank Marek Pechal for all his help on CPW device fabrication and stimulating discussions about the grounding problem in more detail.

We would also like to thank Philipp Kurpiers, Antonio Rubio Abadal and Theo Walter for their help and advice, especially regarding the fitting procedures, for providing their code, and for teaching us the do's and dont's of dipstick measurements.

Bibliography

[1] Markus Aspelmeyer, Tobias J. Kippenberg, and Florian Marquardt. Cavity optomechanics. *Rev. Mod. Phys.*, 86:1391–1452, Dec 2014. 1.2

[2] Inder J Bahl. *Lumped Elements for RF and Microwave Circuits*. Artech House, 2003. (document), 2.8, 2.3.1, 2.3.1, 2.3.1, 2.3.1, 2.10, 2.3.3, 2.3.3

[3] Christopher Eichler. *Experimental Characterization of Quantum Microwave Radiation and its Entanglement with a Superconducting Qubit*. PhD thesis, ETH Zurich, 01 2013. 2.3.5

[4] K. Geerlings, S. Shankar, E. Edwards, L. Frunzio, R. J. Schoelkopf, and M. H. Devoret. Improving the quality factor of microwave compact resonators by optimizing their geometrical parameters. *Appl. Phys. Lett.*, 100(19):192601, 2012. 3.2.4

[5] S. Gevorgian, L. J. P. Linnér, and E. L. Kollberg. CAD models for shielded multilayered CPW. *IEEE T. Microw. Theory.*, 43(2):772, 1995. 2.2.2

[6] M. Göppl, A. Fragner, M. Baur, R. Bianchetti, S. Filipp, J. M. Fink, P. J. Leek, G. Puebla, L. Steffen, and A. Wallraff. Coplanar waveguide resonators for circuit quantum electrodynamics. *J. Appl. Phys.*, 104(6):113904, Dec 2008. 2.2.1, 2.2.4, 3.1, 4.3.2, 6.1.3

[7] J. R. Johansson, G. Johansson, and Franco Nori. Optomechanical-like coupling between superconducting resonators. *Phys. Rev. A*, 90:053833, Nov 2014. 1.2, 6.2.1

[8] Matija Karalic. Characterization of coupled microwave resonator arrays. Master's thesis, ETH Zürich, 01 2014. 4.2

[9] J. Krupka, R.G. Geyer, M. Kuhn, and J.H. Hinken. Dielectric properties of single crystals of Al_2O_3 , $LaAlO_3$, $NdGaO_3$, $SrTiO_3$, and mgo at cryogenic temperatures. *Microwave Theory and Techniques, IEEE Transactions on*, 42(10):1886–1890, 1994. 2.2.2

[10] Paul J. Petersan and Steven M. Anlage. Measurement of resonant frequency and quality factor of microwave resonators: Comparison of methods. *Journal of Applied Physics*, 84(6):3392–3402, 1998. 5.1.1, 5.1.2, 5.1.2, 5.1.2

[11] David M. Pozar. *Microwave engineering*. John Wiley & Sons, Inc., 4th ed. edition, 2011. 2.2.2, 2.4, 2.4.2, 5.1.1

[12] Antonio Rubio Abadal. Josephson parametric amplifiers with lumped-element coupled resonators. Master's thesis, ETH Zürich, 2015. 4.2, 5.1.2, 5.1.2, 5.1.2

[13] Amir H. Safavi-Naeini, Jasper Chan, Jeff T. Hill, Thiago P. Mayer Alegre, Alex Krause, and Oskar Painter. Observation of quantum motion of a nanomechanical resonator. *Phys. Rev. Lett.*, 108:033602, Jan 2012. 1.2.1

[14] Lars Steffen. *Quantum Teleportation and Efficient Process Verification with Superconducting Circuits*. PhD thesis, ETH Zurich, 2013. (document), 2.2.2, 3.1, 3.4, 3.10

[15] Goran Stojanović, Ljiljana Živanov, and Mirjana Damnjanović. Novel efficient methods for inductance calculation of meander inductor. *COMPEL - The international journal for computation and mathematics in electrical and electronic engineering*, 25(4):916–928, 2006. (document), 2.3.2, 2.12

[16] Neereja M. Sundaresan, Yanbing Liu, Darius Sadri, Lszl J. Szocs, Devin L. Underwood, Moein Malekakhlagh, Hakan E. Treci, and Andrew A. Houck. Beyond strong coupling in a multimode cavity. *Physical Review X*, 021035-1, 2015. 1.1

[17] J. D. Teufel, T. Donner, Dale Li, J. W. Harlow, M. S. Allman, K. Cicak, A. J. Sirois, J. D. Whittaker, K. W. Lehnert, and R. W. Simmonds. Sideband cooling of micromechanical motion to the quantum ground state. *Nature*, 475(7356):359–363, July 2011. 1.2, 1.3

[18] M. Tinkham. *Introduction to Superconductivity*. McGraw-Hill International Editions, 1996. 1.1

[19] A.K. Verma, Y.K. Awasthi, and Himanshu Singh. Equivalent isotropic relative permittivity of microstrip on multilayer anisotropic substrate. *International Journal of Electronics*, 96(8):865–875, 2009. 2.2.2

[20] D. J. Wineland and Wayne M. Itano. Laser cooling of atoms. *Phys. Rev. A*, 20(4):1521–1540, October 1979. 1.2

ETH

Eidgenössische Technische Hochschule Zürich
Swiss Federal Institute of Technology Zurich

Declaration of originality

The signed declaration of originality is a component of every semester paper, Bachelor's thesis, Master's thesis and any other degree paper undertaken during the course of studies, including the respective electronic versions.

Lecturers may also require a declaration of originality for other written papers compiled for their courses.

I hereby confirm that I am the sole author of the written work here enclosed and that I have compiled it in my own words. Parts excepted are corrections of form and content by the supervisor.

Title of work (in block letters):

Low Frequency Resonators on Superconducting Chips - A Space-Efficient Lumped Element Design

Authored by (in block letters):
For papers written by groups the names of all authors are required.

Name(s):	**First name(s):**
Lenggenhager	Patrick M.
Mitchell	Bradley

With my signature I confirm that

- I have committed none of the forms of plagiarism described in the 'Citation etiquette' information sheet.
- I have documented all methods, data and processes truthfully.
- I have not manipulated any data.
- I have mentioned all persons who were significant facilitators of the work.

I am aware that the work may be screened electronically for plagiarism.

Place, date	**Signature(s)**
Zurich, 30.09.2015	Bradley Mitchell Patrick Lenggenhager

For papers written by groups the names of all authors are required. Their signatures collectively guarantee the entire content of the written paper.